

3 **Simulated Diagenesis of the Iron-Silica Precipitates in Banded Iron Formations**

4 Isaac L. Hinz¹, Leanne Rossi¹, Chi Ma², and Jena E. Johnson¹

5 ¹Department of Earth and Environmental Sciences, University of Michigan, Ann Arbor, MI
6 48109, USA.

7 ²Division of Geological and Planetary Sciences, California Institute of Technology, Pasadena,
8 91125, CA, USA.

10 **Abstract**

11 Banded Iron Formations, or BIFs, are chemically precipitated sediments that can record Archean
12 ocean geochemistry. BIFs are laminated silica- and iron-rich deposits that host a range of iron(II,
13 III) minerals, including hematite, magnetite, siderite, greenalite, minnesotaite, and stilpnomelane.
14 This diverse mineralogical assemblage reflects secondary mineralization reactions due to
15 diagenesis and/or post-depositional alteration. While petrographic observations of BIFs sparingly
16 contain the iron silicate greenalite, recent evidence of greenalite nanoparticles preserved in early-
17 mineralizing BIF chert suggest this mineral was a primary phase in BIF progenitor sediments.
18 Therefore, it is critical to investigate the formation and alteration of greenalite to constrain the
19 Archean ocean environment and help unravel post-depositional processes. To examine how iron
20 silicates precipitate and then crystallize and/or transform during diagenesis, we simulated these
21 two processes under Archean ocean conditions. We first precipitated a poorly ordered Fe-rich
22 serpentine with subsidiary ferrihydrite at neutral pH by performing in situ Fe(II) oxidation
23 experiments at 25 °C in the presence of silica. Subjected to simulated diagenesis at 80 °C, the
24 rudimentary Fe- phyllosilicate transformed into a crystalline phyllosilicate characterized as 30%

25 cronstedtite-70% greenalite accompanied by magnetite and persistent ferrihydrite. At
26 temperatures ≥ 150 °C, we continued to observe ferrihydrite, increased magnetite formation, and
27 elevated incorporation of Mg into the phyllosilicate as it further recrystallized into Mg-
28 greenalite. Our findings demonstrate a possible formation mechanism of early silicates through
29 partial Fe(II) oxidation and support petrographic observations that magnetite likely mineralizes
30 during diagenesis. Additionally, we suggest that Mg contents in BIF iron phyllosilicates could
31 serve as a tracer for diagenesis, with Mg signaling phyllosilicate-fluid interactions at elevated
32 temperatures. Ultimately, our experiments help reveal how initial iron-silica coprecipitates are
33 altered during diagenesis, providing novel insights into the interpretation of greenalite and
34 magnetite in ancient BIF assemblages.

35

36

37

38

39 Keywords: greenalite, crystallization, magnesium substitution, magnetite, serpentine

40

41

Introduction

42

43

44

45

46

47

48

49

50

Chemical sediments provide an archive of (bio)geochemical processes. The oceans on Archean [4.0-2.5 billion years ago, Ga] Earth were actively precipitating and depositing authigenic chemical sediments, which can therefore serve as a proxy for the ancient marine (bio)geochemistry and signals of the evolution of life (Derry and Jacobson 1990). A prominent example of such sediments are the banded iron formation (BIF) deposits, laminated sedimentary deposits that contain at least 15% iron and commonly also host a high silica content (James 1954). BIFs provide the best record of ancient marine conditions in the Archean ocean, with their chemistry interpreted as reflecting an iron and silica rich system (Klein 2005; Bekker et al. 2014).

51

52

53

54

55

56

57

58

59

60

61

62

63

The presence of BIF deposits in ancient oceans require a mechanism to initially induce chemical precipitation (Holland 1984). Minerals recorded in BIFs contain Fe(II) and Fe(III) with an average oxidation state of Fe^{2.4+} (Klein and Beukes 1992). This is indicative of a partially oxidative environment, the result of biotic and/or abiotic processes in Archean oceans and sediments. Extensive BIF deposition occurred in the Archean ocean, which had little to no molecular oxygen until the Great Oxygenation Event at ~2.3 Ga (Gumsley et al. 2017; Farquhar et al. 2011; Poulton et al. 2021; Johnson and Molnar 2019). Estimates place atmospheric O₂ prior to this rise in oxygen as < 1 ppm or less than ~10^{-5.7} atm (Pavlov and Kasting 2002; Farquhar et al. 2011). A popular hypothesis for the deposition of precursor BIF sediments invoked low levels of dissolved O₂ in the ocean reacting with dissolved Fe²⁺ to consume marine oxygen and form insoluble Fe³⁺ precipitates such as ferric (oxyhydr)oxides (Cloud 1973; Bekker et al. 2014; Konhauser et al. 2017). Others have attributed the generation of BIF progenitor precipitates to anoxygenic Fe²⁺-oxidizing photosynthesis (Hartman 1984; Kappler et al. 2005; Konhauser et al.

64 2002) or reactions between Fe^{2+} and ultraviolet light (Cairns-Smith 1978; Braterman et al. 1983;
65 Bekker et al. 2010).

66 To identify the potential processes responsible for their formation, the iron-rich muds and
67 cherts in BIFs have been intensely investigated. However, the primary BIF sediments
68 experienced physical and chemical alteration as they transformed into sedimentary rock through
69 the process of diagenesis, and most of these rocks were then subject to subsequent post-
70 depositional alteration, fluid flow, and metamorphism (Beukes 1984; Fischer and Knoll 2009;
71 Trendall 2002). Consequently, none of the minerals in BIFs are considered the initial
72 precipitates and BIF deposits are composed of a mineral mixture of chert, hematite, magnetite,
73 iron-rich carbonates, and iron silicates at disequilibrium (Klein 2005; Bekker et al. 2014;
74 Konhauser et al. 2017). This complexity has led to an ongoing debate to determine the most
75 primary mineral(s) associated with BIFs, as only the original precipitates would accurately
76 reflect Archean marine geochemistry and potentially biology.

77 The effects of diagenesis and later alteration complicates the detection of the initial
78 amorphous and/or metastable phases precipitated in Archean oceans, and competing hypotheses
79 suggest two different original BIF precipitates. Earlier models, supplemented by numerous
80 observations of BIFs, pointed to ferric oxides or hydroxides being the primary iron precipitate
81 (James 1954; Cloud 1973; Klein and Beukes 1989; Beukes and Gutzmer 2008; Sun et al. 2015).
82 However, recent studies examined early-mineralizing chert within BIFs that can serve as a
83 barrier to diagenesis, preserving the early assemblage of minerals. These investigations
84 discovered inclusions of iron-rich silicate nanoparticles and suggested these iron silicates were
85 primary minerals from the Archean ocean (Muhling and Rasmussen 2021; Rasmussen et al.
86 2015; Rasmussen et al. 2019). Further characterization of the iron silicate nanoparticles

87 concluded they contained undetectable to < 0.5 atomic% (at.%) quantities of magnesium and
88 ~10-25% Fe(III) (Johnson et al. 2018; Rasmussen et al. 2018). The primary silicates are thus
89 within the solid solution space between greenalite $[(\text{Fe}^{2+}, \text{Mg})_3\text{Si}_2\text{O}_5(\text{OH})_4]$ and cronstedtite
90 $[(\text{Fe}^{2+}, \text{Fe}^{3+}, \text{Mg})_3(\text{Si}, \text{Fe}^{3+})_2\text{O}_5(\text{OH})_4]$, two serpentine group iron silicates with 7 Ångstrom (Å)
91 lattice spacing.

92 These recent observations call for an understanding of the geochemical conditions and
93 mechanism(s) required to form iron silicates under plausible Archean ocean conditions. Previous
94 anoxic experiments conducted at low temperatures of 20-25 °C reported the formation of
95 amorphous to poorly crystalline iron(II)-silica precipitates, proposed to be precursor silicates,
96 when pH was ≥ 7.5 (Farmer et al. 1991; Tosca et al. 2016). The analyses performed on these
97 iron-silica precipitates could not definitively conclude whether these precipitates were a
98 heterogeneous mix of Fe(II) and Si-rich phases or homogenous Fe(II)-silicates (Francisco 2020).
99 However, similar experiments in another study demonstrated that the initial Fe(II)-Si
100 coprecipitates at pH 7.5 could be hydrothermally aged into greenalite-like phases with ~ 7 Å
101 lattice spacing (Hinz et al. 2021). Another concern with the relevance of these experiments is
102 that the pH of ≥ 7.5 used in these experiments was higher than the hypothesized pH of the
103 Archean ocean, which was constrained to pH ~ 6.5 -7.0 by two independent marine and
104 atmospheric geochemical models (Halevy and Bachan 2017; Krissansen-Totten et al. 2018) and
105 considerations of authigenic clay formation (Isson and Planavsky 2018). An additional issue with
106 Fe(II)-silicate precipitation generating the initial BIF sediments is that this Fe(II)-silica saturation
107 mechanism would not account for the low levels of Fe(III) detected in the BIF iron silicate
108 inclusions.

109 To address whether ferric iron can in fact induce precipitation of iron silicates at a more
110 plausible Archean ocean pH of 6.5-7.0, we previously examined the precipitate products
111 resulting from the addition of low amounts of aqueous (aq) Fe(III) to ferrous iron- and silica-rich
112 conditions (Hinz et al. 2021). We found that Fe(III) (aq) triggered the low-temperature
113 precipitation of an amorphous iron- and silica-rich phase accompanied by rare layered silicate-
114 like structures at these more relevant pH values. Earlier studies have simulated diagenesis by
115 hydrothermally aging iron and/or magnesium and silica suspensions at ≥ 60 °C to promote the
116 crystallization of silicates (Baldermann 2014; Mizutani et al. 1991; Tosca et al. 2011). When we
117 hydrothermally aged our Fe(II,III)-silica precipitates at 150 °C, we identified the crystalline
118 products as ~ 7 Å iron phyllosilicates, similar to BIF greenalite but more magnesium-rich, along
119 with additional green rust carbonate, magnetite, hematite, and magnesite (Hinz et al. 2021).

120 The highly oxidized and heterogeneous assemblage that we observed after Fe(III) (aq)
121 additions and 150 °C aging motivated us to explore an alternative precipitation mechanism and
122 hydrothermal aging scheme at several temperatures. In this study, we induced in situ partial
123 Fe(II) oxidation at pH 7 in the presence of silica by bubbling low concentrations of oxygen gas
124 into simulated Archean ocean conditions. The partially-oxidized iron-silica precipitates that
125 formed at room temperature (25 °C) aimed to recreate phases that formed in the Archean water
126 column. To promote crystallization and simulate chemical reactions, we hydrothermally aged
127 these precipitates over the typical diagenetic temperature interval of surface temperatures to 200
128 °C (Brenner et al. 1991; Siever 1986). Similar to previous experimental studies of silicate
129 systems, we aged our initial iron-silica precipitates within anoxic, sealed vessels in sequential
130 steps at 80 °C (Pignatelli et al. 2013; Vacher et al. 2019), 150 °C (Baldermann et al. 2014;
131 Mizutani et al. 1991) and 220 °C (Janecky and Seyfried 1986) and compared these precipitates to

132 low-temperature (25 °C) products. We measured solution chemistry over the course of the
133 simulated diagenesis and characterized the resultant precipitates as they crystallized and
134 transformed.

135

136

Methods

137 Experimental Solution Setup

138 All experiments originated from bulk uniform solutions prepared in 4 L wide mouth jugs
139 at room temperature with 18.2 MΩ-cm ultrapure water. The ultrapure water was boiled before
140 being covered with aluminum foil and purged with pure N₂ gas to deoxygenate the water. Next,
141 the water was brought into a MBraun glovebox consisting of an N₂ atmosphere (< 0.1 ppm O₂)
142 where it was stirred uncapped for at least 72 hours to release any residual oxygen in solution. All
143 solid chemical reagents were weighed outside the glovebox before being transported into the
144 glovebox to be dissolved in deoxygenated water used in experimentation.

145 We prepared a 3.6 L solution in duplicate where first sodium orthosilicate (Na₄SiO₄) was
146 dissolved in the anoxic ultrapure water to a final concentration of 1.1 mM Si. Estimated
147 dissolved silica in Archean seawater was expected to be between ~0.67 mM to an upper limit at
148 amorphous SiO₂ saturation of, ~1.9 mM (Siever 1992; Maliva et al. 2005; Stefurak et al. 2015;
149 Gunnarsson and Arnórsson 2000); we therefore chose an intermediate level between these
150 constraints and below amorphous silica precipitation. The solution was stirred, and the pH was
151 measured with a ThermoFisher Orion Star A221 pH meter outfitted with a Fisherbrand accuCap
152 spear tipped capillary junction pH probe while being adjusted to pH 7 by dropwise additions of 1
153 M hydrochloric acid (HCl). The solution was continuously stirred in the glovebox for 24 hours to

154 allow for the depolymerization of the dissolved silica in solution (Dietzel 2000) before we added
155 other Archean seawater salts.

156 Assuming similar salinity over time, our Archean solution (Table 1) had 400 mM sodium
157 chloride and 7 mM potassium chloride, comparable to the modern ocean (Riley and Chester
158 1971). Archean ocean models have estimated ammonium to be 0.03-10 mM (Stüeken 2016);
159 therefore, we added 10 mM ammonium chloride at the upper end of this range as this reductant
160 may help maintain reducing conditions. The magnesium content in Archean oceans has
161 been estimated to be 10-30 mM (Jones et al. 2015), with processes associated with hydrothermal
162 seawater-oceanic crust interactions decreasing dissolved magnesium in ocean water from today's
163 concentration of ~50 mM (Spencer and Hardie 1990; Halevy and Bachan 2017; Izawa et al.
164 2010). We used the lower estimate and added 10 mM magnesium chloride. A maximum
165 concentration of ~2 mM Fe(II) in Archean oceans has been suggested to be constrained by the
166 supersaturation of ferrous silicates (Jiang and Tosca 2019); we thus set Fe(II) to 1.1 mM.

167 Archean oceans have been estimated to contain 5-30 mM of dissolved inorganic carbon
168 (DIC) (Blättler et al. 2017), and we assume initial pore fluids would have similar concentrations.
169 Additionally, the presence of common organic buffers (HEPES & MOPS) has been shown to
170 impact iron oxidation (Buchholz et al. 2011). Therefore, we added the highest estimate for
171 bicarbonate, 30 mM (Table 1), to both maximize inorganic buffering and account for potential
172 increases in DIC due to organic carbon respiration in the sediments (e.g., Heimann et al, 2010).
173 See Supplemental Materials (SM) for more details.

174 We then mixed the solutions to homogenize any slight chemical differences before
175 apportioning the solution into twelve 610 mL borosilicate glass bottles, wrapped in aluminum
176 foil to prevent any possible ultraviolet (UV) photooxidation of Fe(II). Six of the newly sealed

177 experiments remained in the glovebox to act as ferrous controls. The remaining six identical
178 bottles were removed from the glovebox to be bubbled with low O₂.

179 To partially oxidize the Fe(II) (aq) in situ under simulated Archean ocean conditions, six
180 sealed experimental bottles were equilibrated with N₂ mixed with 49.1 ± 0.9 ppm O₂. Each
181 solution was continuously bubbled with this gas mixture at 3 psi at 25 °C for 90 minutes while
182 outgassing through a separate needle (expanded description in SM). The bottles were transported
183 back into the glovebox and remained resting on their side wrapped in aluminum foil.

184

185 **Initial Fe(II) Oxidation and pH**

186 The bubbled and control experiments were allowed to react and equilibrate horizontally
187 in the glovebox at 25 °C. Each bottle was shaken horizontally three times a week to homogenize
188 the solution. After 19 days, we observed that increases in precipitate quantity had stopped for > 4
189 days and deemed that the Fe(II) (aq) had fully reacted with O₂. We then measured the pH of each
190 control and bubbled experiment (Table 2).

191 To measure the extent of Fe(II) oxidation (reported as Fe(III)/FeT), one of each of the
192 bubbled and control experimental bottles were unsealed and completely acidified with anoxic 4
193 M HCl to a pH of 3 for > 12 hours, after which all visible precipitate was dissolved.
194 Subsequently, the dissolved experimental solutions were analyzed by the ferrozine assay
195 (Stookey 1970; Viollier et al. 2000) to determine the bulk Fe(III)/FeT (Table 3) after
196 equilibration for 19 days at 25 °C. In addition, two precipitate subsamples from the bubbled
197 experiments after 19 days at 25 °C (Fig. 1) were removed and washed three times between
198 centrifuging. One subsample was acidified following the same protocol as described above to
199 complete dissolution before being analyzed by the ferrozine assay (Table 4) while the other

200 subsample was stored and later dissolved and analyzed for its Fe(II) content by the Wilson
201 vanadate method (Tables S1,S2); more details on these assays are below and in SM.

202

203 **Hydrothermal Aging and Subsampling**

204 The remaining four control and four bubbled experiments were mixed to homogenize
205 each condition's solution. The solution, along with any precipitate present, was equally
206 distributed in 15 mL increments into eight separate 22 mL stainless steel gas-tight Parr vessels fit
207 with a PTFE gasket and anoxically sealed. Each bubbled vessel contained ~1-2 grams of
208 precipitate while the control solution had no apparent solids. One of the control and bubbled
209 experiments remained sealed in a Parr vessel within the glovebox at 25 °C for the duration of
210 simulated diagenesis (total of 40 days). Three control and three bubbled experiments in Parr
211 vessels were taken out of the glovebox and placed into a Thermo Scientific™ Heratherm™ oven
212 set at 80 °C to undergo hydrothermal aging.

213 After 7 additional days of hydrothermal aging at 80 °C, one of the control and bubbled
214 Parr vessels were removed from the oven and transferred to the glovebox (Fig. 1). The
215 hydrothermally aged 80 °C vessels were allowed to cool to 25 °C before a pH measurement of
216 the solution was taken (Table 2). If a precipitate was present, the precipitate slurry was
217 centrifuged three times and rinsed with anoxic water with a pH \pm 0.1 of the measured solution
218 value (Table 2) to limit pH-driven reactions after simulated diagenesis while removing excess
219 salts prior to analysis. The precipitate was then subsampled for future analysis and stored in
220 anoxically-sealed Mylar bags within the glovebox at 25 °C. The oven temperature was increased
221 to 150 °C for the remaining Parr vessels.

222 After 7 additional days at 150 °C, another control and bubbled Parr vessel were
223 withdrawn from the oven and taken to the glovebox (Fig. 1). The experimental solutions were
224 again cooled to 25 °C in the glovebox before the pH was measured (Table 2), and any precipitate
225 was rinsed as described above and apportioned for future analysis. After this higher temperature,
226 the control experiment appeared to contain ~0.1 gram of precipitated material while the bubbled
227 experiment had a very similar amount of material as the initial 25 °C starting amount. Finally,
228 the oven temperature for the remaining two Parr vessels was increased to 220 °C.

229 After 7 additional days at 220 °C, the last remaining control and bubbled Parr vessels
230 were transferred to the glovebox (Fig. 1). The solution pH was measured (Table 2), and the
231 precipitate was rinsed and allocated for future analysis. The control and bubbled Parr vessels that
232 remained in the glovebox for the entire 40 days at 25 °C were measured for pH (Table 2), and
233 any precipitate was rinsed and subsampled for future analysis.

234 Using the Act2 program in Geochemist's Workbench (Bethke, 2007), we additionally
235 created stability diagrams for Fe and Mg phases across pH (0-14) and redox space (redox
236 potential, or Eh) to consider the thermodynamically-predicted phases and the potential redox
237 environments that our experimental precipitates experienced during hydrothermal aging.

238

239 **Analytical Sample Preparation and Instrument Parameters**

240 **Iron(II) and (III) Content of Solids**

241 Control and bubbled experiments that produced precipitates were acidified in the
242 glovebox with anoxic 4 M HCl, vigorously shaken, and allowed to dissolve for > 12 hours,
243 following suggestions by Porsch and Kappler (2011) and Braunschweig et al. (2012) to dissolve
244 samples under anoxic conditions at low temperatures to prevent Fe(II) oxidation. However, we

245 used 4 M HCl (instead of 1 M or 6 M HCl) to maintain consistency with the ferrozine assay
246 (Viollier et al. 2000) and subsequently observed complete dissolution of our experimental solids.
247 Dissolved precipitates were analyzed by the ferrozine assay from three subsamples from each
248 experiment to determine the Fe(III)/FeT content (Stookey 1970; Viollier et al. 2000).

249 We additionally evaluated the Fe(II) content of our bubbled experiments following a
250 modified version of the Wilson vanadate method to determine the percent Fe(II) in the samples
251 using a titration-based method (Andrade et al. 2002). See the SM for more details.

252

253 **X-ray Diffraction (XRD)**

254 A precipitate slurry was pipetted as 20 μ L subsamples into Cole-Parmer Kapton tubes
255 with an inner diameter of 1.46 mm and a 0.05 mm wall thickness. Kapton tubes filled with
256 experimental precipitate were allowed to partially dry for 12 hours in the glovebox before both
257 ends of the Kapton tubes were heat sealed shut. The sealed Kapton tubes were protectively
258 placed in 15 mL falcon tubes and heat sealed in mylar bags prior to shipping. Samples were sent
259 to McMaster Analytical X-Ray Diffraction Facility (MAX) for XRD analysis using a Bruker D8
260 DISCOVER cobalt source tube (Co-XRD) with a DAVINCI.DESIGN diffractometer. The
261 diffractometer was set at 35 kV and 45 mA, with a 1 mm slit and 1 mm collimator, with data
262 collected on a VANTEC-500 area detector with a 20 cm working distance. Each sample scan
263 included 4 frames (900 seconds per frame) at 3 separate sample areas over a 2θ range of 10-88°.
264 The 2D frames were collected with DIFFRAC.MEASUREMENT Centre Version 6.5 software
265 and patterns were integrated to 1D using DIFFRAC.EVA Version 4.2.

266

267 **Transmission Electron Microscopy (TEM)**

268 Freshly subsampled precipitates were diluted in anoxic water with a $\text{pH} \pm 0.1$ of the
269 measured condition before pipetting 15 μL of diluted slurry onto lacey carbon coated 300-mesh
270 Cu TEM grids. We allowed residual solution to evaporate prior to analysis, drying in the
271 glovebox under anoxic conditions (< 0.1 ppm O_2), before storing the grids in TEM grid holders
272 and anoxically heat sealing them in a mylar bag. The mylar bags were removed from the
273 glovebox and shipped to Colorado School of Mines, Golden, Colorado, USA for analysis.
274 Samples were examined on a Talos F200X at 200 keV for high-resolution imaging (HR-TEM)
275 up to 0.12 nm, scanning transmission electron microscopy (STEM) imaging up to 0.16 nm, and
276 Super-X window-less electron dispersive X-ray spectroscopy (EDS) analysis. Samples were
277 imaged in high-angle annular dark-field (HAADF) to discern different phases. HR-TEM imaging
278 was used to capture the crystal lattice spacing where the images were analyzed by Fast-Fourier
279 Transformation (FFT) and Inverse FFT (IFFT) using Gatan DigitalMicrograph software.
280 Additional structural data of individual phases was recorded by selected area electron diffraction
281 (SAED). Elemental data was captured by the Talos F200X Super-X EDS detector for a minimum
282 of ten minutes at each location. Bruker ESPRIT software Version 1.9 was used to analyze and
283 quantify the EDS data by the Cliff-Lorimer method with a 1x2 binning. This method converts X-
284 ray counts into raw elemental weight or atomic percent, yielding an accuracy of ± 1 -10% of the
285 collected values. We analyzed representative areas of silicates and oxides to obtain their atomic
286 ratios of cations by first averaging the data from the most isolated particles, then recalculating
287 the oxygen atomic % using cation valence (ignoring any salt-related cations), and finally re-
288 normalizing the data to 100%. We then took the atomic ratios of $(\text{Fe}+\text{Mg})/\text{Si}$ and $\text{Fe}/(\text{Fe}+\text{Mg})$ to
289 gain insights into the silicate character. Image contrast and brightness were adjusted to optimize
290 image clarity.

291

292

Results

293 Solution and Precipitate Chemical Analysis

294 Over the course of this experimental set-up, we measured the pH and extent of iron
295 oxidation in the control and bubbled experiments. The ferrous control experiment after 19 days
296 at 25 °C had a measured pH of 7.14 (Table 2). This experiment had no observable precipitate but
297 after fully acidifying the experimental solution to dissolve any minor solids or colloids, we
298 determined it contained 0.07 Fe(III)/FeT in bulk (Table 3). After a total of 40 days, the 25 °C
299 control had a measured pH of 7.17 (Fig. 2a; Table 2). This room temperature control had no
300 visible color change and yielded no precipitate from which to obtain a Fe(III)/FeT precipitate
301 measurement.

302 Increased hydrothermal temperatures can mimic diagenesis by either inducing higher-
303 temperature reactions such as those that take place during sediment burial and/or simulating the
304 effects of lower diagenetic temperatures over longer geologic time periods (Siever 1986). The
305 control experiment that aged for an additional 7 days at 80 °C had a measured pH of 6.92 (Fig.
306 2a; Table 2). The 80 °C control continued not to display any color change in solution and did not
307 produce a precipitate for Fe(III)/FeT measurement. The control experiment subject to an
308 additional 7 days at 150 °C had a pH of 6.43 (Fig. 2a; Table 2). This 150 °C control did produce
309 a minuscule amount of dark tan-green material that had 0.27 Fe(III)/FeT (Fig. 2b; Table 4). The
310 control experiment aged for an additional 7 days at 220 °C was measured to have a pH of 7.65
311 (Fig. 2a; Table 2). This 220 °C control experiment precipitated a small amount of dark tan-green
312 solid material with 0.32 Fe(III)/FeT (Fig. 2b; Table 4).

313 We induced partial in situ iron(II) oxidation by bubbling trace levels of O₂ gas into
314 Archean ocean solutions for a limited amount of time, and then simulated progressive diagenesis
315 of the partially oxidized precipitates. After 19 days at 25 °C, the acidified and fully dissolved
316 replicate bubbled experiment contained 0.75 Fe(III)/FeT in bulk (dissolved precipitate plus
317 solution) (Table 3). This bubbled experimental solution had a pH of 7.33 and produced a green
318 precipitate, suggesting a Fe(II-III) phase or phases (Velde 2003) (Table 2). Indeed, our ferrozine
319 assay determined that this green precipitate contained 0.48 Fe(III)/FeT and the vanadate assay
320 indicated it was composed of 48% Fe(II) per gram (Tables 4, S2). After an additional 21 days,
321 and 40 days total, the bubbled experiment aged at 25 °C had a solution pH of 7.06 (Fig. 2a;
322 Table 2) and still contained a green precipitate. When we harvested this low-temperature bubbled
323 precipitate, it contained 0.45 Fe(III)/FeT (Fig. 2b; Table 4).

324 The bubbled experiment subject to aging at 80 °C for 7 additional days had a pH of 6.74
325 (Fig. 2a; Table 2) and continued to yield a green precipitate. This 80 °C solid was measured to
326 similarly have 0.45 Fe(III)/FeT and 55.85% Fe(II) by mass (Fig. 2b; Tables 4, S2). The bubbled
327 experiment that was further aged at 150 °C had a measured pH of 6.41 (Fig. 2a; Table 2). This
328 150 °C experiment continued to display a green precipitate and the acidified solid subsample had
329 0.51 Fe(III)/FeT (Fig. 2b; Table 4). While the ratio of Fe(III)/FeT was similar, the % Fe(II) per
330 gram dropped to 32.2% (Table S2). The bubbled experiment that was aged at 220 °C for an
331 additional 7 days had a measured pH of 5.85 (Fig. 2a; Table 2). This bubbled 220 °C experiment
332 produced a slightly darker green-black precipitate with 0.46 Fe(III)/FeT and 27.92% Fe(II)/g
333 (Fig 2b; Tables 4, S2).

334

335 **Thermodynamically Predicted Mineral Phases**

336 The stability diagrams that we constructed, paired with the measured pH values at each
337 step of the hydrothermal aging experiment (Table 2), generated a suite of predicted minerals
338 depending on the redox environment (Eh), which was not directly measured. In the case of
339 magnesium (Fig. S1), the thermodynamically stable phase at pH ~7 and 25 °C or 80 °C was
340 dissolved Mg. The solution pH after continued reaction was within the expanded magnesite
341 stability field at 150 °C, but the higher pH after 220 °C reactions (pH 7.65) shifted the predicted
342 Mg mineral product to a Mg serpentine phase like chrysotile or antigorite. For iron (Fig. S2),
343 siderite or a ferric oxide like goethite should be stable in the 25 °C experiment at pH ~7. At 80
344 °C, there is a small region of magnetite stability as well as the siderite and large goethite stability
345 fields at the experimental pH of ~6.75. With increasing experimental temperature and dropping
346 pH, the magnetite stability field grows while siderite's stable redox and pH space decreases. See
347 SM for more details.

348

349 **Bulk Mineralogy: XRD and Magnetic Response**

350 Control experiments at 150 °C and 220 °C did not produce enough precipitate for
351 analysis by XRD. XRD measurements of bubbled precipitates yielded patterns consistent with
352 several phases (Fig. 3). The bubbled experiment aged for 40 days at 25 °C produced a large and
353 diffuse diffraction peak corresponding to the Kapton tube it was measured in but no other sharp
354 diffraction peaks, suggesting an amorphous to minimally crystalline product (Fig. 3). One broad
355 peak that occurred in the 25 °C precipitate and persisted through the higher-temperature aging
356 treatments may be consistent with ferrihydrite. After 80 °C aging, the bubbled experiment
357 contained three weak diffraction peaks consistent with a serpentine group silicate such as
358 greenalite or cronstedtite and a spinel group oxide like magnetite, as well as two peaks possibly

359 indicating ferrihydrite (Fig. 3). After the 150 °C treatment, bubbled experiments displayed a
360 heightening of the peaks observed at 80 °C along with the formation of additional peaks
361 corresponding to a serpentine group silicate and spinel group oxide (Fig. 3). The bubbled
362 experiment subject to 220 °C aging showed a continued narrowing of the diffraction peaks for a
363 spinel group oxide, reflecting an increase in crystal size and/or crystallinity (Fig. 3). However,
364 the 220 °C experiment showed smaller and less sharp serpentine group peaks and only contained
365 one putative ferrihydrite peak.

366 Control and bubbled experimental precipitates across the range of temperature displayed
367 different degrees of magnetic attraction. The control 150 °C and 220 °C dark tan-green
368 precipitates were both weakly to moderately attracted to the magnet (Fig. 4a & 4b). The bubbled
369 green precipitate at 25 °C after a total of 40 days was not attracted to the magnet (Fig. 4c).
370 However, after 7 days at 80 °C, the green precipitate was weakly attracted to the magnet (Fig.
371 4d). After an additional 7 days at 150 °C, the bubbled green precipitate was strongly attracted to
372 the magnet (Fig. 4e). Seven days of aging at 220 °C produced the darkest green precipitate,
373 which was the most attracted to a magnet compared to all our experimental samples (Fig. 4f).

374

375 **Electron Microscopy Characterization**

376 **High-Temperature Control Experiments.** Unlike the 25 °C and 80 °C control experiments that
377 did not produce a precipitate for analysis, after 7 days at 150 °C, the control contained a
378 miniscule amount of tan precipitate (Fig. 5a). TEM imaging of the 150 °C control revealed
379 abundant ~500 nm clusters composed of a multi-phase mixture: poorly formed tubular spindles,
380 a faint, more amorphous globular phase, and well-ordered crystals with a rod or lath morphology
381 (Fig. 5b-l). The tubular spindles were <10 nm wide and <50 nm long (Fig. 5c-f). They were

382 mainly composed of Mg (17 at.%), Fe (variable but averaging 8.6 at.%), Si (15.5 at.%), and O
383 (58 at.%) (Fig. 5e), with an average $(\text{Fe}+\text{Mg})/\text{Si} = 1.7$, reflecting a composition consistent with a
384 Mg-Fe serpentine group (Table 5). At higher resolution, we observed poorly layered particles
385 with 3-5 layers that were <5 nm wide and <50 nm long and highly susceptible to beam damage
386 (Fig. 5f). We measured the lattice spacing for one of these structures to be 6.9 Å while another
387 structure had 7.2 Å layering (Fig. 5f). Together with the lattice spacing, we tentatively identified
388 the tubular form as an iron-rich Mg-silicate in the serpentine group.

389 In other regions of the 150 °C control, we identified two types of iron oxides. We
390 observed a faint globular phase in lower magnification images (Fig. 5d, arrows) and identified
391 lattice spacings of 1.5 Å (Fig. 5f adjacent to layered phase) as well as 2.3 Å and 2.5 Å (Fig. 5f,g).
392 This poorly crystalline phase was often in an intimate mixture with a rod-like phase (Fig. 5h) but
393 elemental chemistry mapping indicated this phase was primarily iron (31%) and oxygen (54.5%)
394 (Fig. 5i,j, Table 5). These lattice spacings and elemental chemistry are similar to ferrihydrite, a
395 poorly crystalline iron oxide that often forms early after iron is oxidized in neutral waters.
396 Additionally, we imaged more crystalline blunt-edged rods, <20 nm wide and 100-150 nm long,
397 in this sample (Fig. 5h,k). These rods had a lattice spacing of 6.2 Å (Fig. 5k-l) and elemental
398 analysis indicated that they were primarily composed of Fe (28.5 at.%) and O (54.3 at.%) (Fig.
399 6i-6j; Table 5), suggesting an iron oxide mineral. This iron oxide phase also exhibited a lath
400 morphology ~20 nm wide and ~100 nm long (Fig. 6l) with a lattice spacing of 3.2 Å and 6.1 Å
401 (Fig. 5l-I and 5l-II). Neither the blunt edged rods or laths were observed to be degraded by the
402 electron beam during analysis. SAED on a region containing these blunted rods and laths
403 produced a polynanocrystalline pattern (Fig. 5m) consistent with the iron oxide lepidocrocite.

404 The control experiment further aged at 220 °C for 7 additional days also contained a
405 small amount of tan precipitate (Fig. 6a). TEM images of the 220 °C control experiment showed
406 abundant ~100-200 nm long hollow tubes with 0.6-0.8 nm inner diameters and 2-2.8 nm outer
407 diameters (Fig. 6b-d & 6f-g). The elemental chemistry of these tubular structures was primarily
408 Mg (29 at.%), Fe (5 at.%), Si (10 at.%), and O (55 at.%), suggesting they were a magnesium
409 silicate with possibly some Fe(III) substituted for Si (Fig. 6e; Table 5). Along the tube axis, we
410 were able to capture two separate instances of 7.2 Å lattice spacing and higher order lattice
411 planes of 3.6 Å (004) and 2.4 Å (006) (Fig. 6f & 6g-I). Another tube at a different orientation
412 captured the 4.3 Å (111) lattice plane of this phase (Fig. 6g-II). SAED of the control 220 °C
413 experiment on a broad region composed mostly of tubes produced diffraction halos, suggesting a
414 poorly crystalline phase (Fig. 6j). This tubular phase had an elemental chemistry, lattice
415 spacings, and SAED pattern consistent with a precursor form of the fibrous magnesium
416 serpentine, chrysotile.

417 TEM analyses of the 220 °C control experiment also captured a ~100 nm wide globular
418 phase (Fig. 6h). The elemental data of this phase indicated that it primarily contained Fe (28
419 at.%) and O (54 at.%) (Fig. 6h-i; Table 5), suggesting an iron oxide. Additionally, the broad
420 SAED of the 220 °C control experiment had distinct diffraction planes (manifesting as dots) that
421 corresponded to the lattice spacings of 2.9 Å (220), 1.4 Å (440), and 1.0 Å (553) (Fig. 6j). These
422 lattice planes captured by SAED in tandem with an elemental chemistry rich in iron and oxygen
423 lead us to tentatively identify the globular phase as a spinel group iron oxide; notably, these
424 lattice spacings align well with maghemite. With its globular morphology rather than the platelet
425 morphology of the magnetite in the bubbled experiments (see below), it is possible that this
426 phase was not magnetite but instead was a different spinel group oxide like maghemite.

427

428 **Bubbled Experiments: Iron Oxide Phases.** We imaged the bubbled precipitates at temperatures
429 25-220 °C using TEM. All our bubbled experiments appeared to produce both a phyllosilicate
430 phase (see below) and a poorly crystalline iron oxide phase, while experiments aged at >80 °C
431 additionally contained a more crystalline iron oxide.

432 The subtle oxide phase observed in all the bubbled experiments appeared as a faint
433 globular phase in the background matrix (Fig. 7). SAED on the 25 °C assemblage produced a
434 diffuse halo pattern corresponding to 1.3 Å, 1.5 Å, and 2.6 Å lattice spacings (Fig. 8g). These
435 diffuse SAED halos reflect the formation of a poorly crystalline phase, consistent with the lack
436 of peaks by XRD (Fig. 3), but the spacings are typical of ferrihydrite. Using HR-TEM, we
437 observed that the globular phase had a recurring lattice spacing of ~2.5-2.6 Å (Fig. 7c,e,g,i). We
438 also observed a ~1.6 Å spacing (Fig. 7g). EDS spectra that included this phase suggested it was
439 rich in Fe, O, and Si (Table 5, Table S3). Together, we suggest our data points to Si-rich
440 ferrihydrite, which has major spacings at 1.5, 1.6, 2.5, and 2.6 Å in its 2-line and 6-line forms
441 (Michel et al, 2007).

442 Starting at 80 °C and increasingly at higher temperatures, we also observed a more
443 crystalline triangular or polygonal platelet phase in the bubbled experiments that we ultimately
444 identified as magnetite (Fig. 8). TEM and HR-TEM analysis of the bubbled precipitates aged at
445 80 °C, 150 °C, and 220 °C captured ~50-100 nm wide platelets with a characteristic 4.7 Å basal
446 spacing (Fig. 8c,f,h) along with additional lattice planes by FFT (Fig. 8c-I,f-I,h-I) corresponding
447 to a spinel group phase such as magnetite. For example, after 150 °C aging, FFT on an area with
448 platelets revealed lattice spacing planes of 4.8 Å (111), 2.4 Å (222), 1.6 Å (333), and 2.5 Å (311)
449 (Fig. 8f-I), very similar to the spacings expected for spinel group phases. FFT analysis on a

450 platelet-rich region after 220 °C aging (Fig. 8h-I) showed these same lattice spacings and
451 additionally a spacing at 1.7 Å (422), which is also observed in spinels. We were able to obtain a
452 SAED pattern of a platelet-rich region in this 220 °C-aged sample as well (Fig. 8i), which was
453 again consistent with a spinel group mineral like magnetite. We captured elemental data from a
454 region containing the platelet phase and observed that it was mainly composed of Fe (22 at.%), O
455 (56 at.%), and Si (11 at.%) (Fig. 8g; Table 5). We attribute the higher-than-expected
456 measurement of Si in this spinel group phase to be the result of adsorbed Si (Philippini et al.
457 2006). The lattice spacing of the platelet paired with the elemental chemistry rich in Fe and O, in
458 addition to the strong magnetic reaction of the bubbled and hydrothermally-aged precipitates
459 (Fig. 4d-f), was most consistent with identifying this platelet phase as magnetite.

460

461 **Bubbled Experiments: Silicate Phase.** Analysis of the 40-day-old 25 °C precipitate revealed
462 abundant poorly layered spindly particles that were ~2-4 nm wide and ~20 nm long (Fig. 9).
463 EDS of the layered precipitates from three separate locations yielded a compositional range of
464 17.5-21 at.% Fe, 17-19 at.% Si, 1-3 at.% Mg, 59-60 at.% O (Fig. 9e-g; Table 5). From this data,
465 we calculated an average (Fe+Mg)/Si ratio of 1.2 for these poorly layered particles (Table 5).
466 These structures were highly susceptible to beam damage, but we were able to capture four
467 representative particles, each with a maximum of 3-4 layers that had an approximate lattice
468 spacing of ~7.2-7.7 Å (Fig. 9h-I,II & 9i-I,II) measured by IFFT. The observed morphological,
469 structural, and elemental data suggested this phase was a Fe-rich incipient serpentine.

470 In the bubbled experimental precipitate aged at 80 °C for 7 additional days, TEM
471 imaging revealed layered crystals with a variable degree of ordering (Fig. 10). We observed
472 ~100 nm wide and ~300-700 nm long bladed structures and measured their lattice fringe at 7.2 Å

473 (Fig. 10b-e,h). TEM also revealed multiple instances of a triangular-trapezoidal form (Fig. 10b-
474 arrows,f-g) where the well-ordered regions had a 7.0 Å lattice fringe (Fig. 10j-I). The bladed and
475 triangular-trapezoidal structures together exhibited an average elemental chemistry with low Mg
476 (1.6 at.%) and a range of (Fe+Mg)/Si of 2.11-2.43, consistent with an iron silicate within the
477 cronstedtite-greenalite solid solution (Fig. 10d-e,g; Table 5). The large remaining portion of the
478 structure exhibited multiple crystal defects restricting the number of ordered layers (Fig. 10i-j);
479 however, we did measure a 7.2 Å lattice fringe in this region as well (Fig. 10i-I). SAED on an
480 area containing the bladed and trapezoidal structures produced recurring diffraction planes
481 congruous with a serpentine group silicate (Fig. 9k).

482 TEM analysis of the bubbled sample at 150 °C for an additional 7 days displayed well-
483 ordered layered structures ~100-200 nm long and ~10-50 nm wide (Fig. 11b-d). Using elemental
484 data from three regions containing layered structures (Fig. 11e-g), we calculated an average
485 (Fe+Mg)/Si = 1.8 with a Mg content of 4.5 at.% (Table 5). We measured 7.2-7.3 Å basal spacing
486 in two separate particles from one image (Fig. 11h, 11h-I). In another instance, a well-ordered
487 layered particle was in the proper orientation to capture both its basal lattice spacing of 7.1 Å
488 (Fig. 11i) and 24 Å superlattice (Fig. 11i-I). Collectively, the TEM data demonstrated that these
489 structures were greenalite-like minerals.

490 TEM of the bubbled experiment after 7 days at 220 °C revealed ~400 nm clusters of well-
491 ordered layered structures that were ~20-60 nm wide and ~100 nm long (Fig. 12). In general, we
492 observed fewer well-order layered structures at 220 °C compared to lower temperatures, but the
493 structures were highly crystalline. We determined that the basal lattice spacing was 7.1 Å in two
494 separate layered particles (Fig. 12c,f), with one of these particle orientations also capturing a ~21
495 Å superlattice (Fig. 12f-I). We also measured the elemental composition of these layered

496 structures in two regions (Fig. 12d,g), and observed that the particles remained Fe and Si rich but
497 the average Mg content had increased to 10% (Table 5). This data enabled us to calculate the
498 average (Fe+Mg)/Si of 1.7 (Table 5). Collectively, the TEM data demonstrated that these
499 structures were greenalite-like minerals.

500

501 **Synthesis of Experimental Results**

502 Our ferrous control experiment set at pH 7 with 1:1 Fe:Si did not produce an observable
503 precipitate from solution either at low temperature nor upon 80 °C hydrothermal aging. At 150
504 °C, we observed temperature-induced precipitation of an abundant but poorly ordered ~7 Å
505 Mg(Fe)-silicate along with ferrihydrite and lepidocrocite (Fig. 5). There may also have been a
506 magnetic mineral like magnetite in this assemblage since this assemblage showed a magnetic
507 response (Fig. 4a). Additional aging at 220 °C of the ferrous control mainly produced chrysotile
508 nanotubes and a spinel group iron-oxide that was potentially maghemite (Fig. 6). During
509 hydrothermal aging, the ferrous solution decreased in pH as temperature increased and minerals
510 precipitated. The 25 °C solution had a pH of 7.17, which decreased to pH 6.74 at 80 °C, and
511 further decreased to pH 6.43 at 150 °C (Fig. 2a; Table 2). This decrease in pH can be attributed
512 to the formation of an Fe(III) (hydr)oxide, such as the lepidocrocite and ferrihydrite that we
513 observed. Additionally, the precipitation of silicate phases will take up hydroxide ions and
514 release protons, also dropping the pH (Zolotov 2014).

515 Low O₂ bubbled experiments examined in situ Fe(II) oxidation at pH 7 in the presence of
516 silica produced a partially oxidized (~45% Fe(III)/FeT and ~48% Fe(II)/g) precipitate (Fig. 2b).
517 After 40 days at 25 °C, we characterized this low-temperature assemblage as abundant precursor
518 Fe-rich serpentine and ancillary ferrihydrite (Fig. 7a-c, Fig. 9). Aging these precipitates at 80 °C

519 produced a well-layered iron silicate and magnetite alongside ferrihydrite (Figs. 7d-e, 8a-c, 10).
520 Continued hydrothermal aging at 150 °C and 220 °C crystallized well-ordered greenalite with
521 incorporated Mg, more magnetite, and some persistent ferrihydrite (Figs. 7f-i, 8d-I, 11, 12; Table
522 5). These higher-temperature assemblages also contained lower Fe(II), ~30% by mass compared
523 to ~50% at ≤ 80 °C, although their Fe(III)/FeT ratio remained about the same (Table 4). With
524 increasing temperature, the experimental solution pH decreased from a pH of 7.33 at 25 °C down
525 to pH 5.85 at 220 °C (Fig. 2a; Table 2). The continued decrease in pH can be attributed to the
526 formation and recrystallization of the iron silicate and magnetite phases, similar to the control
527 experiments.

528

529

Discussion

530 Impacts of Temperature on Ferrous Controls at Circumneutral pH

531 Our ferrous experiments under simulated silica-rich Archean ocean conditions at pH 7
532 did not produce a precipitate at low temperature. Other studies with Archean-relevant Fe(II) and
533 Si concentrations produced iron(II) silicates at 25 °C, but only when the pH was elevated to ≥ 7.5
534 (Tosca et al. 2016; Farmer et al. 1991; Hinz et al. 2021). During the Fe(II) hydrolysis process,
535 silica inhibits Fe(II) polymerization, resulting in smaller clusters of octahedral Fe(II) and a
536 kinetic barrier to precipitation (Doelsch et al. 2002; Francisco et al. 2020). Our observations of a
537 lack of precipitation at ≤ 80 °C supports previous studies' findings that a higher pH is required to
538 induce iron(II) silicate formation under ferrous conditions at low temperature.

539

540

541

However, our ferrous experiment at 25 °C did contain a trace amount of Fe(III) (bulk
Fe(III)/FeT = 0.07, Table 3), which would be expected to precipitate at circumneutral pH. The
presence of any Fe(III) suggests there may have been slight O₂ contamination or a trace Fe(III)

542 impurity in all of our experiments. Even with this minor amount of Fe(III), the lack of precipitate
543 in this experiment is surprising since Fe(III) is highly insoluble at circumneutral pH and readily
544 precipitates as ferric oxides or Fe(II,III) phases from solution. Under these Fe, Si, and pH
545 conditions, we suspect that Fe(III) aqueous complexes, such as Fe(III)-Si, Fe(OH)_2^+ ,
546 Fe(OH)CO_3 , and FeCl^{2+} (Steffansoon 2007; Perrson 2018), hosted the measured Fe(III). Kinsela
547 et al. (2016) has shown the presence of silica—even an order of magnitude below the 1.1 mM Si
548 used in this study—hinders Fe(II) oxidation at circumneutral pH. Therefore, the absence of
549 precipitate at low temperature and 80 °C in our ferrous control experiments was likely the result
550 of the presence of high dissolved silica and insufficient Fe(III) to trigger precipitation of ferric
551 oxides or Fe(II,III) silicates as observed by Hinz et al. 2021.

552 Increased temperatures can influence chemical processes and induce mineral
553 precipitation, and our results showed precipitation in the control precipitates at 150 °C that
554 preferentially incorporated the trace dissolved Fe(III). At this elevated temperature, the control
555 precipitate contained 0.27 Fe(III)/FeT (Fig. 2b; Table 4). Indeed, we observed that Fe(III) oxides,
556 ferrihydrite and lepidocrocite, formed at 150 °C under almost entirely ferrous conditions (Fig.
557 5d,h-m). Soluble Fe(II) in the presence of poorly crystalline Fe(III) oxides like ferrihydrite is
558 capable of catalyzing the reductive dissolution and secondary mineralization of more crystalline
559 ferric oxides such as lepidocrocite or goethite (Burton et al. 2007; Cornell and Schwertmann
560 2003; Hansel et al. 2005; Nitschmann 1938; Pedersen et al. 2005). Therefore, we hypothesize
561 that the higher 150 °C temperature promoted the precipitation of ferric oxides from trace
562 dissolved Fe(III), and, in the presence of abundant Fe(II), these initial oxides partially
563 recrystallized into the lepidocrocite that we observed.

564 Our observations of the ferrous control experiment aged at 150 °C also revealed the
565 precipitation of a magnesium-rich silicate phase. While poorly ordered, the magnesium silicate
566 with ~9 at.% iron was notably the most abundant phase and manifested in distinctive tube-like
567 structures with rarely captured 6.9-7.2 Å basal spacing (Fig. 5c-f, Table 5). This spacing suggests
568 that the control liquid precipitated a poorly formed serpentine group magnesium silicate with
569 substantial incorporation of iron. Thermodynamic modeling indicates that chrysotile and
570 antigorite, two types of serpentine group Mg silicates, are only stable at pH ~7-7.5 and higher at
571 150 °C (Fig. S1c), suggesting there may be local regions of higher pH to promote precipitation
572 of this observed phase despite the bulk solution pH (6.4, Table 2) being unfavorable for this
573 silicate group.

574 After 220 °C aging, our ferrous control experiment was predominantly composed of
575 chrysotile nanotubes and a globular iron oxide (Fig. 6). The widespread fibrous chrysotile at 220
576 °C suggests the transformation of the poorly formed 150 °C Mg-silicate to the more crystalline
577 chrysotile mineral. The elemental analysis of the chrysotile nanotubes showed they included 5
578 at.% Fe (Fig. 6e; Table 5). Chrysotile has been reported to host 2-3 weight % (wt.%) Fe (Bowes
579 and Farrow 1997), where Fe(II) or Fe(III) are capable of being substituted into the octahedral site
580 but only Fe(III) can be incorporated into the tetrahedral site (Walter et al. 2019). The
581 incorporation of Fe into the chrysotile structure could have been aided by dissolution-
582 reprecipitation reactions during the crystallization of Mg silicates into chrysotile. These reactions
583 mineralizing chrysotile and releasing OH groups likely also buffered the solution to sit within the
584 chrysotile stability field, including raising the pH to the 7.65 that we measured in this experiment
585 (Table 2; Figs. 2a, S1d; Trittschack et al. 2014). There may have been substantial incorporation
586 of Fe(III) into the chrysotile structure upon 220 °C aging, similar to what occurs during

587 serpentinization (Evans 2008; Tuto et al. 2021). Indeed, the Fe(III) content of the bulk
588 precipitate increased from 27% at 150 °C to 32% at 220 °C. Alternatively, it is possible that most
589 of the iron in chrysotile was Fe(II), and the majority of the measured 32% Fe(III) in solids was
590 associated with the iron oxide.

591

592 **In Situ Fe(II) Oxidation at Circumneutral pH and 25 °C**

593 Broadly, our trace O₂ bubbling experiments highlight that in situ Fe(II) oxidation in the
594 presence of silica produces an Fe-rich poorly ordered serpentine at pH 7 and 25 °C. The presence
595 of a small proportion of Fe(III) under silica-rich conditions has been shown to induce
596 precipitation of iron-rich solids, including silicate phases (Hinz et al. 2021). This low-Fe(III)
597 trigger provides an alternative mechanism for the formation of precursor Fe-rich serpentine at
598 low temperatures and the predicted lower pH of the Archean ocean. However, in our previous
599 study, adding Fe(III) (aq) in the presence of silica at pH 7 and 25 °C produced mainly an
600 amorphous phase with rare silicates, with a bulk iron redox state of 0.89 Fe(III)/FeT (Hinz et al.
601 2021). Yet here, in situ Fe(II) oxidation at pH 7 induced the formation of a more ferrous
602 assemblage that was 48% Fe(II)/g and contained approximately equimolar Fe(II) and Fe(III),
603 with more abundant Fe-rich precursor silicate phases alongside ferrihydrite at 25 °C (Figs. 7a-c,
604 9; Table 4).

605 Similar to the control experiments, our results from bubbled experiments suggested that
606 there was additional Fe(III) dissolved in the solution. The acidified 25 °C bubbled solution-
607 precipitate combination contained much higher Fe(III), measuring 0.75 Fe(III)/FeT, compared to
608 the 0.48 Fe(III)/FeT in solids (Tables 3,4). This higher bulk measurement possibly reflects that a
609 portion of the Fe(III) was in Fe(III) aqueous complexes, such as Fe(III)-Si, Fe(OH)₂⁺,

610 $\text{Fe}(\text{OH})\text{CO}_3$, and FeCl^{2+} , similar to what we suspect occurred with the minor amount of Fe(III)
611 in the control experiment solutions (Steffansoon 2007; Perrson 2018). The additional Fe(III)
612 measured in solution could also be attributed to colloidal Fe(II,III) phases such as silicates, green
613 rusts, or Fe(III) oxides. The Fe(III) discrepancy between the precipitate compared to bulk redox
614 state implies that we cannot discount the impact that these dissolved or colloidal Fe(III) sources
615 may have on mineral formation. However, the precipitates from bubbled experiments all
616 exhibited a consistent proportion of Fe(III) per total iron, ranging from 0.45-0.51 Fe(III)/FeT,
617 regardless of aging conditions or temperatures (Fig. 2b; Table 4). This Fe(III) stability in bubbled
618 experiments across all temperatures suggests that there was not substantial incorporation of
619 Fe(III) (aq) into the solid with increasing temperature.

620

621 **Products from Simulated Diagenesis of Partially Oxidized Iron-Silica Precipitates**

622 In tandem, the bulk redox measurements of the solids suggest that there was substantial
623 dissolution-reprecipitation during the hydrothermal aging incubations. Mineral crystallization
624 often involves a precursor metastable or amorphous phase dissolving as a more crystalline phase
625 precipitates (Ruiz-Agudo et al. 2017; DeYoreo et al. 2015, 2022). The % Fe(II)/g measurements,
626 which show a ~20% drop between 80 and 150 °C (Table 4), indicate there was dissolution of at
627 least some of the previously-precipitated Fe(II) between these temperatures. However, the
628 unchanging Fe(III)/FeT (Table 4) suggest that a similar proportion of Fe(III) also dissolved
629 during 80 °C to 150 °C recrystallization and/or transformation. While our TEM data shows that a
630 portion of the Fe(II) recrystallized in more ordered phyllosilicate and magnetite phases, some of
631 the Fe(III) appears to have remained in ferrihydrite since we observed ferrihydrite at all
632 temperatures (Fig. 7). At minimum, a fraction of the initial ferrihydrite was resistant to reactions

633 with dissolved Fe(II) and/or transformation to other iron oxides as is typically seen (Huang et al.
634 2021) and as we observed in our control experiments. Adsorbed silica may have protected some
635 ferrihydrite from further reactions even up to 220 °C, consistent with other experiments that
636 found Si-rich ferrihydrite does not transform to secondary phases until >500 °C (Rzepa et al.
637 2016; Campbell et al. 2002). Additionally, the presence of bicarbonate buffer can impede the
638 secondary transformation of ferrihydrite, potentially through bicarbonate forming aqueous
639 complexes with Fe(II) or by adsorbing to ferrihydrite (Hansel et al. 2005).

640 While iron-rich silicates were present under all hydrothermal conditions (more on their
641 transformations below), the appearance of magnetite at 80 °C and higher temperatures (Fig. 8)
642 revealed that this Fe(II,III) oxide was a secondary phase that mineralized during the simulated
643 diagenetic conditions. The increase in magnetite crystallization with higher temperatures was
644 denoted by sharpened peaks in the XRD patterns (Fig. 3), TEM observations (Fig. 8), and
645 strengthening magnetic attraction (Fig. 4d-f). Magnetite most likely formed due to reactions
646 between Fe(II) and ferrihydrite, in a known process when there is sufficient Fe(II) to adsorb to
647 the ferrihydrite and induce transformation into magnetite (Tronc et al. 1992; Hansel et al. 2003,
648 2005). Presumably a portion of the 25 °C ferrihydrite was not as protected by adsorbed silica or
649 bicarbonate and was able to adsorb and react with dissolved Fe(II). However, an alternative (or
650 additional) mechanism to form magnetite could stem from initial Fe(II,III) phyllosilicates
651 relinquishing ferric iron to form more ferrous silicates and magnetite, similar to reactions
652 described by Zolotov (2014) and potentially explaining the deterioration of greenalite-like XRD
653 peaks between 150 and 220 °C (Fig. 3).

654

655 **Effects of Simulated Diagenesis on Fe(II,III) Silicates**

656 After in situ Fe(II) oxidation at 25 °C, the initial precursor iron silicates crystallized into
657 a well-ordered iron serpentine phase upon hydrothermal aging (Fig. 13). To identify and
658 understand the identity and extent of crystallization of iron phyllosilicates, we must examine
659 their observed characteristics. The structural measurements, including the 7 Å basal spacing, of
660 the silicate products in bubbled experiments indicated they were serpentine group silicates,
661 which are composed of alternating silica tetrahedral layers and metal-bound octahedral layers.
662 The chemistry we observed in bubbled silicate products at all temperatures indicated that the
663 principal metal ion was Fe, pointing to a serpentine group iron silicate, either Fe(II) greenalite or
664 Fe(II,III) cronstedtite. One way to differentiate cronstedtite from greenalite stems from the fact
665 that the Fe(II) in greenalite has a misfit between the tetrahedral and octahedral layers, resulting in
666 a modulated structure (Guggenheim et al. 1982; Guggenheim and Eggleton 1998). This
667 superlattice structure of greenalite has a ~23 Å modulation (Guggenheim et al. 1982;
668 Guggenheim and Bailey 1989; Guggenheim and Eggleton 1998; Rasmussen et al. 2021; Johnson
669 et al. 2018), in contrast to the ~17 Å superlattice periodicity of the Mn(II) serpentine endmember
670 caryopilite and the 33-38 Å modulation of the Mg serpentine antigorite (Guggenheim et al 1982;
671 Capitani and Mellini 2004). Conversely, the Fe(III) within the cronstedtite structure has a smaller
672 ionic radius than Fe(II) or Mg. The Fe(III) substitution for silica at the tetrahedral site stabilizes
673 the layered configuration and restricts structural modulation; therefore, the ~23 Å superlattice is
674 not observed in cronstedtite (Caruso and Chernosky 1979; Wicks and O'Hanley 2018; Hybler,
675 2000). Additionally, the Fe(III) substitution at the silica tetrahedra site in cronstedtite increases
676 its ideal (Fe+Mg)/Si ratio to 4 compared to 1.5 for greenalite, providing an additional way to
677 identify the iron serpentine mineralogy.

678 We can thus place the experimental silicates at various temperatures along the greenalite-
679 cronstedtite solid solution, as well as infer their Fe(III) content, by their measured (Fe+Mg)/Si
680 ratio. To characterize the composition of the silicates and where they fall along the cronstedtite-
681 greenalite solid solution, we used the defined formulas for both endmembers, greenalite with
682 possible Mg substitution $[(\text{Fe}^{2+}, \text{Mg})_3\text{Si}_2\text{O}_5(\text{OH})_4]$ and cronstedtite with possible Mg substitution
683 $[(\text{Fe}^{2+}, \text{Fe}^{3+}, \text{Mg})_3(\text{Si}, \text{Fe}^{3+})_2\text{O}_5(\text{OH})_4]$, and compared the (Fe+Mg)/Si ratio of our experimental
684 products against the idealized ratios from mineral formulas. Mg-containing greenalite
685 $(\text{Fe}^{2+}, \text{Mg})_3\text{Si}_2\text{O}_5(\text{OH})_4$ would have a (Fe+Mg)/Si ratio of 1.5, while Mg-containing cronstedtite
686 $(\text{Fe}^{2+}, \text{Fe}^{3+}, \text{Mg})_3(\text{Si}, \text{Fe}^{3+})_2\text{O}_5(\text{OH})_4$ would have a ratio of 4. The silicate precipitated at 25 °C had
687 an (Fe+Mg)/Si of 1.2, below the theoretical (Fe+Mg)/Si ratio for greenalite of 1.5 due to its
688 elevated Si content (Table 5). This higher Si content in the initial, poorly ordered form of iron
689 silicates was similarly observed in prior studies (Tosca et al. 2016; Hinz et al. 2021).

690 At 80 °C, we observed the crystallization of a 7 Å iron silicate (Fig. 10c,e,h; Table 5)
691 with much lower relative Si, averaging a (Fe+Mg)/Si of 2.3, which falls between cronstedtite and
692 greenalite. Additionally, the 80 °C phyllosilicate displayed a pseudo-triangular morphology and
693 lacked any indication of a superlattice despite being well-crystallized (Fig. 10b-arrows,f,j),
694 consistent with observations from similar cronstedtite formation studies (Pignatelli et al. 2013
695 and Vacher et al. 2019). Based on the defined endmember formulas, the bubbled 80 °C layered
696 precipitate with (Fe+Mg)/Si of ~2.3 was characterized as a 30% cronstedtite and 70% greenalite
697 solid solution (Table 5). Assuming all the measured Fe+Mg was Fe^{2+} or Fe^{3+} , which is not too
698 inaccurate considering this sample only contained 1.6 at.% Mg on average, and assuming that
699 this Fe was equally split between the two redox states, our calculated proportion of cronstedtite
700 would suggest that this 80 °C-crystallized phyllosilicate contained approximately 15% Fe(III).

701 Therefore, there appears to be a transition from a high-Si iron silicate at low temperatures
702 to a crystalline phase within the solid solution between Fe(II) greenalite and Fe(II,III)
703 cronstedtite at 80 °C. Intriguingly, the $\Delta G_{\text{formation}}^{\circ}$ for cronstedtite has been found to be favorable
704 at temperatures < 120 °C, high Fe/Si ratios, and circumneutral pH, similar to our experimental
705 conditions (Zolotov 2014; Pignatelli et al. 2013, 2014; Vacher et al. 2019). The thermodynamic
706 stability field for cronstedtite under our solution conditions shrinks between 25 °C and 80 °C,
707 with the redox and pH space filled largely by magnetite (Fig. S2a-b). These stability field
708 predictions may support a transformation of initial poorly ordered Fe(II,III) silicate, i.e. a
709 precursor cronstedtite-greenalite, into magnetite. Yet the pH of our experimental solutions was
710 lower than the pH range of the stability field of cronstedtite, and our observations of
711 ferrihydrite—a precursor of goethite—would suggest that the redox environment was more
712 oxidizing than the highly reducing conditions required by cronstedtite or greenalite (Fig. S2a-b).
713 These contradictions suggest that our experimental precipitates formed in heterogeneous
714 microenvironments where pH and the redox state (commonly measured as Eh) were variable.
715 The differences between the thermodynamic predictions and our observations also suggest that
716 the kinetics of these precipitation and crystallization processes determine the solid assemblage,
717 even after 7 days of 80 °C hydrothermal aging.

718 In contrast to lower-temperature silicates, additional recrystallization and mineralization
719 at higher temperatures (150-220 °C) aging produced an iron phyllosilicate characteristic of the
720 greenalite endmember. In the abundant layered forms, we continued to observe 7 Å spacing
721 typical of a serpentine group silicate (Figs. 11h-i, 12c,f). Yet the layered phase at these
722 temperatures exhibited a 21-24 Å superlattice (Figs. 11i-I & 12f-I) and (Fe+Mg)/Si of 1.7-1.8
723 (Table 5), close to ideal greenalite and not congruent with cronstedtite. Our results thus indicate

724 that cronstedtite was not present in experiments ≥ 150 °C, supporting the thermodynamic
725 predictions (Fig S2) and hypothesis that cronstedtite does not form at higher temperatures
726 (Vacher et al. 2019). Instead, we suggest the more Fe(III)-rich cronstedtite-greenalite that
727 initially crystallized at 80 °C dissolved and partially reprecipitated into a more endmember Fe(II)
728 greenalite at ≥ 150 °C. With the narrowing stability field for greenalite, we again speculate that
729 local environments persisted—perhaps buffered by the initial silicates—where higher pH and
730 more reducing redox conditions enabled the continued presence of greenalite. However, we note
731 that the greenalite appeared less abundant in both TEM imaging at 220 °C and in the sample's
732 XRD pattern, perhaps suggesting that greenalite had indeed partially dissolved or transformed.

733 Not only did the higher-temperature aging result in greenalite mineralization, but we
734 observed an increasing incorporation of Mg in the layered silicate. While the phyllosilicate had
735 minimal magnesium at 25-80 °C (~1.5-2 at.% Mg), Mg increased to 4.5 at.% at 150 °C and 10
736 at.% at 220 °C (Fig. 13; Table 5). As there was only trace Mg in the lower temperature
737 precipitates, this incorporated magnesium almost certainly originated from the solution, which
738 contained 10 mM Mg to be analogous to Archean seawater. The large extent of Mg incorporation
739 into the silicate was comparable to the 11-15 at.% Mg in 150 °C-aged experimental iron silicates
740 either formed under ferrous conditions at pH 7.5 or triggered by a small amount of ferric iron at
741 pH 6.5-7 (Hinz et al. 2021).

742 Our simulated diagenesis experiments suggest that, similar to today (Berg et al. 2019;
743 Sun et al. 2016), a sink for magnesium in Archean time may have been in the Mg enrichment of
744 silicates during sedimentary diagenesis and burial. For example, studies of the Amazon delta
745 sediments have shown that Mg is incorporated in secondary silicate clays during simulated and
746 observed diagenesis (Michalopoulos and Aller 1995; Rude and Aller, 1989). The process of clay

747 mineralization in the sediments, also known as ‘reverse weathering’ or clay authigenesis, is
748 supported by the uptake of Mg in much of today’s marine sediments and concomitant depletion
749 of Mg in pore waters (Sayles, 1979; Gieskes 1975; Sun et al. 2016).

750 This precipitation and/or incorporation of Mg during high temperature recrystallization is
751 also reminiscent of the behavior of Mg in hydrothermal vent systems and the flanks of mid-
752 ocean ridges, where Mg is largely removed from heated circulating seawater to form Mg-silicate
753 phases (German and Seyfried 2014; Mottl and Wheat 1994). Experiments simulating this
754 seawater-basalt interaction at 250-290 °C observed the precipitation of the Mg aluminosilicate
755 saponite (Voigt et al 2020). In our experiments, Mg likely remained dissolved until sufficiently
756 high temperatures because of the very stable Mg hydration complex (Hostetler and Christ 1968;
757 Sayles and Fyfe 1973) and then the Mg partitioned into the iron silicate as its kinetic barriers to
758 mineralization were overcome by increased temperature. Notably, our observation of increasing
759 Mg with continued aqueous alteration also follows the pattern of Mg enrichment during the
760 aqueous alteration inferred in carbonaceous CM chondrites (Suttle et al. 2021; McSween 1979;
761 Tomeoka et al. 1989; Howard et al. 2011) and increasing Mg in serpentines during
762 serpentinization alteration reactions (e.g., Evans 2008; Beard et al. 2009). Our experimental
763 results therefore support the hypothesis that Mg will exchange for Fe with progressive alteration,
764 following the chondrite alteration model of McSween (1979) and Tomeoka et al. (1989).

765

766

Implications

767 This study demonstrates that iron phyllosilicates will precipitate under simulated Archean
768 ocean conditions as a result of in situ Fe(II) oxidation. We showed that in situ Fe(II) oxidation in
769 the presence of silica at pH 7 can precipitate poorly ordered iron-rich phyllosilicates with a very

770 low Mg content at 25 °C. At 80 °C, these precipitates crystallized into low-Mg iron
771 phyllosilicates in the solid solution between greenalite and cronstedtite. These 80 °C iron silicate
772 nanoparticles appeared remarkably similar to inclusions in early-forming BIF chert that are
773 composed of low-Fe(III) greenalite with negligible Mg (Rasmussen et al. 2019; Johnson et al.
774 2018). With increasing temperatures simulating further diagenesis, our experimental
775 phyllosilicates transformed into a more greenalite-like mineral with less Fe(III) but considerably
776 more Mg. In contrast, the low (< 0.5 at.%) Mg content of iron phyllosilicate inclusions in BIF
777 cherts suggests that they were likely formed under low temperatures, then preserved and isolated
778 in chert, restricting further reaction with Mg-containing seawater.

779 In the context of the BIF rock record, our observations could also provide insights into
780 how diagenesis in the presence of Mg-rich fluids affects the crystallization and transformation of
781 other BIF iron silicates as well. Broader scale BIF studies of iron silicates (greenalite,
782 minnesotaite, and stilpnomelane) that are not preserved in chert can have a large range of Mg
783 content (0.6-6.7 weight % MgO) within the silicate phases (Klein 2005; Klein 1974; Floran and
784 Papike 1978). Our data would suggest the more elevated (> ~2 at.%) levels of Mg in these
785 silicates derived from continued higher-temperature alteration of the initial BIF sediments,
786 without the isolation provided by early-mineralizing chert. Consistent with this idea,
787 observations of the silicate-bearing facies collected from separate localities with different
788 degrees of BIF diagenesis were measured to have different Fe:Mg ratios (Floran and Papike
789 1978).

790 The formation of magnetite that we observed after the simulated diagenesis of iron
791 silicates at high temperatures of ≥ 150 °C illuminates how BIF sediments may be expected to
792 transform into secondary minerals. Magnetite is ubiquitous in BIF facies, but its origin is not

793 well understood (Klein 2005). Previous petrographic studies of BIFs have shown that most, if not
794 all, of the magnetite in these formations is a relatively late-formed mineral (Goodwin 1956;
795 Laberge 1964; French 1968, 1973; Han 1982; Kaufman et al. 1990; Kaufman 1996; Beukes and
796 Gutzmer 2008; Rasmussen and Muhling 2018). Magnetite in BIF deposits thus most likely
797 represents diagenetic and/or post depositional alteration, obscuring the primary mineral(s) from
798 which the magnetite derived. Intriguingly, petrographic observations support magnetite replacing
799 early iron silicate granules (French 1968; Klein 1974; Floran and Papike 1978; Rasmussen and
800 Muhling, 2018). We demonstrated that the simulated diagenesis of Fe(II,III) silicates and
801 ferrihydrite at ≥ 80 °C produces magnetite (Fig. 8). These experiments thus suggest that iron-rich
802 silicate phases are a possible precursor to diagenetic magnetite in BIFs, potentially providing
803 experimental evidence for petrographic observations of iron silicates altering to magnetite.

804 Other experimental studies have also indicated that magnetite is a secondary mineral that
805 forms during diagenesis. Magnetite can be formed as a product of microbial Fe(III) respiration
806 (Lovley et al. 1987), a process that is hypothesized to occur in BIF sediments (e.g., Walker,
807 1984; Konhauser et al. 2005; Fischer and Knoll, 2009). While few studies have simulated burial
808 diagenesis of BIFs, Posth et al. (2013) subjected ferrihydrite and glucose to 14 days of 170 °C
809 and 1200 bars to investigate the diagenetic transformation of Fe(III) oxides and microbial
810 biomass. These experiments also produced magnetite, which they linked to organic carbon-
811 induced reduction of the ferric iron, except when the ferrihydrite was silica-coated. Our results
812 suggest alternative pathways exist to form magnetite during diagenesis: hydrothermally aging
813 mixed Fe(II,III) precipitates and/or Fe(III) phases in the presence of aqueous Fe(II) additionally
814 forms magnetite in a process unrelated to organic carbon. Moreover, silica was present in our

815 solutions in the same concentration as ferrous iron; therefore, it appears that silica does not
816 always prevent the formation of magnetite during high-temperature mineralization.

817 Our simulated diagenesis experiments therefore demonstrate the effects of diagenesis on
818 iron silicates, with clear changes to the Fe(III) and Mg content, and ultimately provide support
819 for a secondary origin of magnetite and guidance on how to interpret the magnesium content in
820 iron-rich silicates in the BIF record.

821

822

Acknowledgements

823 We acknowledge funding from NASA Exobiology (J.E.J., Award #80NSSC18K1060) and NSF
824 Geobiology and Low-Temperature Geochemistry (J.E.J., Award # 2142509) that supported this
825 work. We especially thank David Diercks (Colorado School of Mines, Golden, Colorado, USA)
826 for assistance with TEM imaging and analyses and Victoria Jarvis (McMaster University,
827 Hamilton, Ontario, Canada) for performing the Co-XRD measurements.

828

829

References

- 830 Andrade, S., Hypolito, R., Ulbrich, H.G.J., and Silva, M.L. (2002) Iron(II) oxide determination
831 in rocks and minerals. *Chemical Geology*, 182, 85-89.
- 832 Baldermann, A., Dohrmann, R., Kaufhold, S., Nickel, C., Letofsky-Papst, I., and Dietzel, M.
833 (2014) The Fe-Mg-saponite solid solution series – a hydrothermal synthesis study. *Clay*
834 *Minerals*, 49, 391–415.
- 835 Beard, J.S., Frost, R.B., Fryer, P., McCaig, A., Searle, R., Ildefonse, B., Zinin, P., and Sharma,
836 S.K. (2009) Onset and Progression of Serpentinization and Magnetite Formation in
837 Olivine-rich Troctolite from IODP Hole U1309D. *Journal of Petrology*, 50, 387-403.

- 838 Beard, J.S., and Frost, R.B. (2017) The stoichiometric effects of ferric iron substitutions in
839 serpentine from microprobe data. *International Geology Review*, 59, 5-6.
- 840 Bekker, A., Slack, J.F., Planavsky, N., Krapez, B., Hofmann, A., Konhauser, K.O., and Rouxel,
841 O.J. (2010) Iron Formation: The Sedimentary Product of a Complex Interplay among
842 Mantle, Tectonic, Oceanic, and Biospheric Processes. *Economic Geology*, 105, 467–508.
- 843 Bekker, A., Planavsky, N.J., Krapež, B., Rasmussen, B., Hofmann, A., Slack, J.F., Rouxel, O.J.,
844 and Konhauser, K.O. (2014) Iron Formations: Their Origins and Implications for Ancient
845 Seawater Chemistry. In *Treatise on Geochemistry* pp. 561–628. Elsevier.
- 846 Berg, R.D. Solomon, E.A., and Teng, F. (2019) The role of marine sediment diagenesis in the
847 modern oceanic magnesium cycle. *Nature Communications*, 10, 4371.
- 848 Bethke, C.M. (2007) *Geochemical and Biogeochemical Reaction Modeling*, 2nd ed. Cambridge
849 University Press, Cambridge.
- 850 Beukes, N.J. (1984) Sedimentology of the Kuruman and Griquatown Iron-formations, Transvaal
851 Supergroup, Griqualand West, South Africa. *Precambrian Research*, 24, 47–84.
- 852 Beukes, N.J., and Gutzmer, J. (2008) Origin and Paleoenvironmental Significance of Major Iron
853 Formations at the Archean-Paleoproterozoic Boundary. In *Banded Iron Formation-*
854 *Related High-Grade Iron Ore*. Society of Economic Geologists.
- 855 Blättler, C.L., Kump, L.R., Fischer, W.W., Paris, G., Kasbohm, J.J., and Higgins, J.A. (2017)
856 Constraints on ocean carbonate chemistry and pCO₂ in the Archaean and
857 Palaeoproterozoic. *Nature Geoscience*, 10, 41–45.
- 858 Bowes, D.R., and Farrow, C.M. (1997) Major and trace element compositions of the UICC
859 standard asbestos samples. *American Journal of Industrial Medicine*, 32, 592–594.
- 860 Braterman, P.S., Cairns-Smith, A.G., and Sloper, R.W. (1983) Photo-oxidation of hydrated Fe²⁺

- 861 significance for banded iron formations. *Nature*, 303, 163–164.
- 862 Braunschweig, J., Bosch, J., Heister, K., Kuebeck, C., and Meckenstock, R.U. (2012)
- 863 Reevaluation of colorimetric iron determination methods commonly used in
- 864 geomicrobiology. *Journal of Microbiological Methods*, 89, 41-48.
- 865 Brenner, R.L., Ludvigson, G.A, Scal, R., and Dogen, A.U. (1991) Diagenetic modeling of
- 866 siliciclastic systems; status report. *Kansas State Geological Survey*, 233, 123-137.
- 867 Buchholz, A., Laskov, C., and Haderlein, S.B. (2011) Effects of Zwitterionic Buffers on Sorption
- 868 of Ferrous Iron at Goethite and Its Oxidation by CCl_4 . *Environmental Science &*
- 869 *Technology*, 45, 3355–3360.
- 870 Burton, E.D., Bush, R.T., Sullivan, L.A., and Mitchell, D.R.G. (2007) Reductive transformation
- 871 of iron and sulfur in schwertmannite-rich accumulations associated with acidified coastal
- 872 lowlands. *Geochimica et Cosmochimica Acta*, 71, 4456–4473.
- 873 Cairns-Smith, A.G. (1978) Precambrian solution photochemistry, inverse segregation, and
- 874 banded iron formations. *Nature*, 276, 807–808.
- 875 Campbell, A.S., Schwertmann, U., Stanjek, H., Friedl, J., Kyek, A., and Campbell, P.A. (2002)
- 876 Si Incorporation into Hematite by Heating Si–Ferrihydrite. *Langmuir*, 18, 7804–7809.
- 877 Capitani, G., and Mellini, M. (2004) The modulated crystal structure of antigorite: The $m = 17$
- 878 polysome. *American Mineralogist*, 89, 147-158.
- 879 Caruso, L.J., and Chernosky, J.V. (1979) The Stability of Lizardite. *Canadian Mineralogist*, 17,
- 880 757-769.
- 881 Cloud, P. (1973) Paleocological Significance of the Banded Iron-Formation. *Economic*
- 882 *Geology*, 68, 1135–1143.
- 883 Cornell, R.M., and Schwertmann, U. (2003) *The Iron Oxides: Structure, Properties, Reactions,*

- 884 Occurrences and Uses, 1st ed. Wiley.
- 885 D19 Committee (2016) D859-16 Test Method for Silica in Water. ASTM International.
- 886 Derry, L.A., and Jacobsen, S.B. (1990) The chemical evolution of Precambrian seawater:
887 Evidence from REEs in banded iron formations. *Geochimica et Cosmochimica Acta*, 54,
888 2965–2977.
- 889 De Yoreo, J.J., Gilbert, P.U.P.A., Sommerdijk, N.A.J.M., Penn, R.L., Whitlam, S., Joester, D.,
890 Zhang, H., Rimer, J.D., Navrotsky, A., Banfield, J.F., and others (2015) Crystallization
891 by particle attachment in synthetic, biogenic, and geologic environments. *Science*, 349,
892 aaa6760.
- 893 De Yoreo, J.J., Nakouzi, E., Jin, B., Chun, J., and Mundy, C.J. (2022) Spiers Memorial Lecture:
894 Assembly-based pathways of crystallization. *Faraday Discussions*, 235, 9–35.
- 895 Dietzel, M. (2000) Dissolution of silicates and the stability of polysilicic acid. *Geochimica et*
896 *Cosmochimica Acta*, 64, 3275–3281.
- 897 Doelsch, E., Rose, J., Masion, A., Bottero, J.Y., Nahon, D., and Bertsch, P.M. (2002) Hydrolysis
898 of Iron(II) Chloride under Anoxic Conditions and Influence of SiO_4 Ligands. *Langmuir*,
899 18, 4292–4299.
- 900 Evans, B.W. (2008) Control of the products of serpentinization by $\text{Fe}^{2+}\text{Mg}_{-1}$ exchange potential
901 of olivine and orthopyroxene. *Journal of petrology*, 49, 1873-1887.
- 902 Falini, G., Foresti, E., Gazzano, M., Gualtieri, A.F., Leoni, M., Lesci, I.G., and Roveri, N. (2004)
903 Tubular-Shaped Stoichiometric Chrysotile Nanocrystals. *Chemistry - A European*
904 *Journal*, 10, 3043–3049.
- 905 Farmer, V.C., Krishnamurti G.S.R., and Huang, P.M. (1991) Synthetic allophane and layer-
906 silicate formation in $\text{SiO}_2\text{-Al}_2\text{O}_3\text{-FeO-Fe}_2\text{O}_3\text{-MgO}$ systems at 23C and 89C in a

- 907 calcareous environment. *Clays Clay Mineralogy*, 36, 561-570.
- 908 Farquhar, J., Zerkle, A.L., and Bekker, A. (2011) Geological constraints on the origin of
909 oxygenic photosynthesis. *Photosynthesis Research*, 107, 11–36.
- 910 Fischer, W.W., and Knoll, A.H. (2009) An iron shuttle for deepwater silica in Late Archean and
911 early Paleoproterozoic iron formation. *Geological Society of America Bulletin*, 121, 222-
912 235.
- 913 Floran, R.J., and Papike, J.J. (1978) Mineralogy and Petrology of the Gunflint Iron Formation,
914 Minnesota-Ontario: Correlation of Compositional and Assemblage Variations at Low to
915 Moderate Grade. *Journal of Petrology*, 19, 215–288.
- 916 Francisco, P.C.M., Mitsui, S., Ishidera, T., Tachi, Y., Doi, R., and Shiwaku, H. (2020)
917 Interaction of FeII and Si under anoxic and reducing conditions: Structural characteristics
918 of ferrous silicate co-precipitates. *Geochimica et Cosmochimica Acta*, 270, 1–20.
- 919 French, B.M. (1968) Progressive contact metamorphism of the Biwabik Iron Formation, Mesabi
920 Range, Minnesota. *Minnesota Geologic Survey*, 64,103.
- 921 French, B.M. (1973) Mineral Assemblages in Diagenetic and Low-Grade Metamorphic Iron-
922 Formation. *Economic Geology*, 68, 1063–1074.
- 923 Fuchs, Y., Linares, J., and Mellini, M. (1998) Mossbauer and infrared spectrometry of lizardite-
924 1T from Monte Fico, Elba. *Physical Chemical Minerals*, 26, 111-115.
- 925 German, C.R., and Seyfried, W.E. (2014) Hydrothermal Processes. In H.D. Holland and K.K.
926 Turekian, Eds., *Treatise on Geochemistry (Second Edition)* pp. 191–233. Elsevier,
927 Oxford.
- 928 Gieskes, J.M. (1975) Chemistry of Interstitial Waters of Marine Sediments. *Annual Review of*
929 *Earth and Planetary Sciences*, 3, 433-453.

- 930 Goodwin, A.M. (1956) Facies relations in the Gunflint iron formation [Ontario]. Economic
931 Geology, 51, 565–595.
- 932 Guggenheim, S., and Bailey, S.W. (1989) An occurrence of a modulated serpentine related to the
933 greenalite-caryopilite series. American Mineralogist, 74, 637-641.
- 934 Guggenheim, S., Bailey, S.W., Eggleton, R.A., and Wilkes, P. (1982). Structural aspects of
935 greenalite and related minerals. Canadian Mineralogist, 20, 1-18.
- 936 Guggenheim, S., and Eggleton, R.A. (1998) Modulated crystal structures of greenalite and
937 caryopilite: a system with a long range, in-plane structural disorder in the tetrahedral
938 sheet. Canadian Mineralogist, 36, 163-179.
- 939 Gumsley, A.P., Chamberlain, K.R., Bleeker, W., Söderlund, U., de Kock, M.O., Larsson, E.R.,
940 and Bekker, A. (2017) Timing and tempo of the Great Oxidation Event. Proceedings of
941 the National Academy of Sciences, 114, 1811–1816.
- 942 Gunnarsson, I., and Arnórsson, S. (2000) Amorphous silica solubility and the thermodynamic
943 properties of H_4SiO_4 in the range of 0° to 350°C at Psat. Geochimica et Cosmochimica
944 Acta, 64, 2295–2307.
- 945 Haavik, C., Stølen, S., Fjellvåg, H., Hanfland, M., and Häusermann, D. (2000) Equation of state
946 of magnetite and its high-pressure modification: Thermodynamics of the Fe-O system at
947 high pressure. American Mineralogist, 85, 514–523.
- 948 Halevy, I., and Bachan, A. (2017) The geologic history of seawater pH. Science, 355, 1069–
949 1071.
- 950 Han, T.M. (1982) Iron Formations of Precambrian Age: Hematite-Magnetite Relationships in
951 Some Proterozoic Iron Deposits - A Microscopic Observation. Ore Genesis.
- 952 Hansel, C.M., Benner, S.G., Neiss, J., Dohnalkova, A., Kukkadapu, R.K., and Fendorf, S. (2003)

- 953 Secondary mineralization pathways induced by dissimilatory iron reduction of
954 ferrihydrite under advective flow. *Geochimica et Cosmochimica Acta*, 67, 2977–2992.
- 955 Hansel, C.M., Benner, S.G., and Fendorf, S. (2005) Competing Fe(II)-Induced Mineralization
956 Pathways of Ferrihydrite. *Environmental Science & Technology*, 39, 7147–7153.
- 957 Hartman, H. (1984) The evolution of photosynthesis and microbial mats: A speculation on the
958 banded iron formations. In Cohen, Y., Castenholz, R.W., and Halvorson, H.O. *Microbial*
959 *Mats: Stromatolites*. Alan R Liss, 449-453.
- 960 Heimann, A., Johnson, C.M., Beard, B.L., Valley, J.W., Roden, E.E., Spicuzza, M.J., and
961 Beukes, N.J. (2010) Fe, C, and O isotope compositions of banded iron formation
962 carbonates demonstrate a major role for dissimilatory iron reduction in ~2.5Ga marine
963 environments. *Earth and Planetary Science Letters*, 294, 8–18.
- 964 Hinz, I.L., Nims, C., Theuer, S., Templeton, A.S., and Johnson, J.E. (2021) Ferric iron triggers
965 greenalite formation in simulated Archean seawater. *Geology*, 49, 905–910.
- 966 Holland, H.D. (1984) *The Chemical Evolution of the Atmosphere and Oceans*. Princeton
967 University Press, 598.
- 968 Hostetler, P.B., and Christ, C.L. (1968) Studies in the system MgO-SiO₂-CO₂-H₂O(l): The
969 activity-product constant of chrysotile. *Geochimica et Cosmochimica Acta*, 32, 485-497.
- 970 Howard, K.T., Benedix, G.K., Bland, P.A., and Cressey, G. (2011) Modal mineralogy of CM
971 chondrites by X-ray diffraction (PSD-XRD): Part 2. Degree, nature and settings of
972 aqueous alteration. *Geochemica et Cosmochimica Acta*, 75, 2735-2751.
- 973 Huang, J., Jones, A., Waite, T.D., Chen, Y., Huang, X., Rosso, K.M., Kappler, A., Mansor, M.,
974 Tratnyek, P.G., and Zhang, H. (2021) Fe(II) Redox Chemistry in the Environment.
975 *Chemical Reviews*, 121, 8161–8233.

- 976 Hybler, J., Petricek, A., Durovic, I.S., and Smrcek, L. (2000) REFINEMENT OF THE
977 CRYSTAL STRUCTURE OF CRONSTEDTITE-IT. *Clays and Clay Minerals*, 8.
- 978 Isson, T.T., and Planavsky, N.J. (2018) Reverse weathering as a long-term stabilizer of marine
979 pH and planetary climate. *Nature*, 560, 471–475.
- 980 Izawa, M.R.M., Nesbitt, H.W., MacRae, N.D., and Hoffman, E.L. (2010) Composition and
981 evolution of the early oceans: Evidence from the Tagish Lake meteorite. *Earth and
982 Planetary Science Letters*, 298, 443–449.
- 983 James, H.L. (1954) Sedimentary Facies of Iron-Formation. *Economic Geology*, 49, 235-293.
- 984 Janecky, D.R., and Seyfried, W.E. (1986) Hydrothermal serpentinization of peridotite within the
985 ocean crust: Experimental investigations of mineralogy and major element chemistry.
986 *Geochimica et Cosmochimica Acta*, 50, 1357-1378.
- 987 Jiang, C.Z., and Tosca, N.J. (2019) Fe(II)-carbonate precipitation kinetics and the chemistry of
988 anoxic ferruginous seawater. *Earth and Planetary Science Letters*, 506, 231–242.
- 989 Johnson, J.E., and Molnar, P.H. (2019) Widespread and Persistent Deposition of Iron Formations
990 for Two Billion Years. *Geophysical Research Letters*, 46, 3327–3339.
- 991 Johnson, J.E., Muhling, J.R., Cosmidis, J., Rasmussen, B., and Templeton, A.S. (2018) Low-
992 Fe(III) Greenalite Was a Primary Mineral From Neoproterozoic Oceans. *Geophysical
993 Research Letters*, 45, 3182–3192.
- 994 Jones, C., Nomosatryo, S., Crowe, S.A., Bjerrum, C.J., and Canfield, D.E. (2015) Iron oxides,
995 divalent cations, silica, and the early earth phosphorus crisis. *Geology*, 43, 135–138.
- 996 Kappler, A., Pasquero, C., Konhauser, K.O., and Newman, D.K. (2005) Deposition of banded
997 iron formations by anoxygenic phototrophic Fe(II)-oxidizing bacteria. *Geology*, 33, 865.
- 998 Kaufman, A.J. (1996) Geochemical and mineralogic effects of contact metamorphism on banded

- 999 iron-formation: an example from the Transvaal Basin, South Africa. *Precambrian*
1000 *Research*, 79, 171–194.
- 1001 Kaufman, A.J., Hayes, J.M., and Klein, C. (1990) Primary and diagenetic controls of isotopic
1002 compositions of iron-formation carbonates. *Geochimica et Cosmochimica Acta*, 54,
1003 3461–3473.
- 1004 Kinsela, A.S., Jones, A.M., Bligh, M.W., Pham, A.N., Collins, R.N., Harrison, J.J., Wilsher,
1005 K.L., Payne, T.E., and Waite, T.D. (2016) Influence of Dissolved Silicate on Rates of
1006 Fe(II) Oxidation. *Environmental Science & Technology*, 50, 11663–11671.
- 1007 Klein, C. (1974) Greenalite, Stilpnomelane, Minnesotaite, Crocidolite and Carbonates in a very
1008 Low-Grade Metamorphic Precambrian Iron-Formation. *Canadian Mineralogist*, 12, 475-
1009 498.
- 1010 Klein, C. (2005) Some Precambrian banded iron-formations (BIFs) from around the world: Their
1011 age, geologic setting, mineralogy, metamorphism, geochemistry, and origins. *American*
1012 *Mineralogist*, 90, 1473–1499.
- 1013 Klein, C., and Beukes, N.J. (1989) Geochemistry and sedimentology of a facies transition from
1014 limestone to iron-formation deposition in the early Proterozoic Transvaal Supergroup,
1015 South Africa. *Economic Geology*, 84, 1733–1774.
- 1016 Klein, C., and Beukes, N.J. (1992) Models for iron-formation deposition. Cambridge University
1017 Press, 147-151.
- 1018 Konhauser, K.O., Hamade, T., Raiswell, R., Morris, R.C., Grant Ferris, F., Southam, G., and
1019 Canfield, D.E. (2002) Could bacteria have formed the Precambrian banded iron
1020 formations? *Geology*, 30, 1079.
- 1021 Konhauser, K.O., Newman, D.K., and Kappler, A. (2005) The potential significance of microbial

- 1022 Fe(III) reduction during deposition of Precambrian banded iron formations. *Geobiology*,
1023 3, 167–177.
- 1024 Konhauser, K.O., Planavsky, N.J., Hardisty, D.S., Robbins, L.J., Warchola, T.J., Haugaard, R.,
1025 Lalonde, S.V., Partin, C.A., Oonk, P.B.H., Tsikos, H., and others (2017) Iron formations:
1026 A global record of Neoproterozoic to Palaeoproterozoic environmental history. *Earth-*
1027 *Science Reviews*, 172, 140–177.
- 1028 Krissansen-Totton, J., Arney, G.N., and Catling, D.C. (2018) Constraining the climate and ocean
1029 pH of the early Earth with a geological carbon cycle model. *Proceedings of the National*
1030 *Academy of Sciences*, 115, 4105–4110.
- 1031 LaBerge, G.L. (1964) Development of Magnetite in Iron-Formations of the Lake Superior
1032 Region. *Economic Geology*, 59, 1313-1342.
- 1033 Lafuente, B., Downs, R.T., Yang, H., Stone, N. (2015). The power of databases: the RRUFF
1034 project. *Highlights in Mineralogical Crystallography*, 1-30.
- 1035 Lovley, D.R., Stolz, J.F., Nord, G.L., and Phillips, E.J.P. (1987) Anaerobic production of
1036 magnetite by a dissimilatory iron-reducing microorganism. *Nature*, 330, 252–254.
- 1037 Maliva, R.G., Knoll, A.H., and Simonson, B.M. (2005) Secular change in the Precambrian silica
1038 cycle: Insights from chert petrology. *Geological Society of America Bulletin*, 117, 835.
- 1039 McSween, H.Y. (1979) Are Carbonaceous Chondrites Primitive or Processed? A Review.
1040 *Reviews of Geophysics and Space Physics*, 17, 1059-1078.
- 1041 Michalopoulos, P., and Aller, R.C. (1995) Rapid Clay Mineral Formation in Amazon Delta
1042 Sediments: Reverse Weathering and Oceanic Elemental Cycles. *Science*, 270, 614–617.
- 1043 Michel, F.M., Ehm, L., Antao, S.M., Lee, P.L., Chupas, P.J., Liu, G., Strongin, D.R., Schoonen,
1044 M.A.A., Phillips, B.L., and Parise, J.B. (2007) The Structure of Ferrihydrite, a

- 1045 Nanocrystalline Material. *Science*, 316, 1726–1729.
- 1046 Mizutani, T. (1991) Synthesis of 1:1 and 2:1 Iron Phyllosilicates and Characterization of their
1047 Iron State by Mössbauer Spectroscopy. *Clays and Clay Minerals*, 39, 381–386.
- 1048 Mottl, M.J., and Wheat, C.G. (1994) Hydrothermal circulation through mid-ocean ridge flanks:
1049 Fluxes of heat and magnesium. *Geochimica et Cosmochimica Acta*, 58, 2225-2237.
- 1050 Muhling, J.R., and Rasmussen, B. (2020) Widespread deposition of greenalite to form Banded
1051 Iron Formations before the Great Oxidation Event. *Precambrian Research*, 339, 105619.
- 1052 Nitschmann, H. (1938) Reaktionslenkung durch Keime. Beobachtungen bei der Oxydation von
1053 Eisen in Eisen(II)-sulfatlösung. *Helvetica Chimica Acta*, 21, 1609–1618.
- 1054 O’Hanley, D.S. (1996) *Serpentinites: Records of Tectonic and Petrologic History*, Oxford
1055 University Press, 78, 137-138.
- 1056 O’Hanley, D.S., and Dyar, M.D. (1993) The composition of lizardite 1T and the formation of
1057 magnetite in serpentinites. *American Mineralogist*, 78, 391-404.
- 1058 O’Hanley, D.S., and Dyar, M.D. (1998) The composition of chrysotile and its relationship with
1059 lizardite. *The Canadian Mineralogist*, 36, 727-739.
- 1060 Pavlov, A.A., and Kasting, J.F. (2002) Mass-Independent Fractionation of Sulfur Isotopes in
1061 Archean Sediments: Strong Evidence for an Anoxic Archean Atmosphere. *Astrobiology*,
1062 2, 27–41.
- 1063 Pedersen, H.D., Postma, D., Jakobsen, R., and Larsen, O. (2005) Fast transformation of iron
1064 oxyhydroxides by the catalytic action of aqueous Fe(II). *Geochimica et Cosmochimica*
1065 *Acta*, 69, 3967–3977.
- 1066 Persson, I. (2018) Ferric Chloride Complexes in Aqueous Solution: An EXAFS Study. *Journal of*
1067 *Solution Chemistry*, 47, 797–805.

- 1068 Philippini, V., Naveau, A., Catalette, H., and Leclercq, S. (2006) Sorption of silicon of magnetite
1069 and other corrosion products of iron. *Journal of Nuclear Materials*, 348, 60-69.
- 1070 Pignatelli, I., Mugnoili, E., Hybler, J., Mosser-Ruck, R., Cathelineau, M., and Michau, N.
1071 (2013) A multi-technique characterization of cronstedtite synthesized by iron-clay
1072 interaction in a step-by-step cooling procedure. *Clays and Clay Minerals*, 61, 277-289.
- 1073 Pignatelli, I., Bourdelle, F., Bartier, D., Mosser-Ruck, R., Truche, L., Mugnaioli, E., and Michau,
1074 N. (2014) Iron-clay interactions: Detailed study of the mineralogical transformation of
1075 claystone with emphasis on the formation of iron-rich T-O phyllosilicates in a step-by-
1076 step cooling experiment from 90 °C to 40 °C. *Chemical Geology*, 387, 1-11.
- 1077 Porsch, K., and Kappler, A. (2011) FeII oxidation by molecular O₂ during HCl extraction.
1078 *Environmental Chemistry*, 8, 190–197.
- 1079 Posth, N.R., Köhler, I., D. Swanner, E., Schröder, C., Wellmann, E., Binder, B., Konhauser,
1080 K.O., Neumann, U., Berthold, C., Nowak, M., and others (2013) Simulating Precambrian
1081 banded iron formation diagenesis. *Chemical Geology*, 362, 66–73.
- 1082 Postma, D. (1993) The reactivity of iron oxides in sediments: A kinetic approach. *Geochimica et*
1083 *Cosmochimica Acta*, 57, 5027–5034.
- 1084 Poulton, S.W., Bekker, A., Cumming, V.M., Zerkle, A.L., Canfield, D.E., and Johnston, D.T.
1085 (2021) A 200-million-year delay in permanent atmospheric oxygenation. *Nature*, 592,
1086 232–236.
- 1087 Rasmussen, B., and Muhling, J.R. (2018) Making magnetite late again: Evidence for widespread
1088 magnetite growth by thermal decomposition of siderite in Hamersley banded iron
1089 formations. *Precambrian Research*, 306, 64–93.
- 1090 Rasmussen, B., Krapež, B., and Muhling, J.R. (2015) Seafloor silicification and hardground

- 1091 development during deposition of 2.5 Ga banded iron formations. *Geology*, 43, 235–238.
- 1092 Rasmussen, B., Muhling, J.R., Tosca, N.J., and Tsikos, H. (2019) Evidence for anoxic shallow
1093 oceans at 2.45 Ga: Implications for the rise of oxygenic photosynthesis. *Geology*, 47,
1094 622–626.
- 1095 Rasmussen, B., Muhling, J.R., and Fischer, W.W. (2021) Greenalite Nanoparticles in Alkaline
1096 Vent Plumes as Templates for the Origin of Life. *Astrobiology*, 21, 246–259.
- 1097 Riley, J.P. and Chester, R. (1971) *Introduction to marine chemistry*. Academic Press, London.
- 1098 Rude, P.D. and Aller, R.C. (1989) Early diagenetic alteration of lateritic particle coatings in
1099 Amazon continental shelf sediment. *Journal of Sedimentary Research*, 59, 704–716.
1100 <https://doi.org/10.1306/212F9052-2B24-11D7-8648000102C1865D>
- 1101 Ruiz-Agudo, E., Putnis, C.V., and Rodríguez-Navarro, C. (2017) Reactions between minerals
1102 and aqueous solutions. In W. Heinrich and R. Abart, Eds., *Mineral reaction kinetics:
1103 Microstructures, textures, chemical and isotopic signatures* Vol. 16. European
1104 Mineralogical Union and Mineralogical Society of Great Britain and Ireland.
- 1105 Rzepa, G., Pieczara, G., Gaweł, A., Tomczyk, A., and Zalecki, R. (2016) The influence of
1106 silicate on transformation pathways of synthetic 2-line ferrihydrite. *Journal of Thermal
1107 Analysis and Calorimetry*, 125, 407–421.
- 1108 Sayles, F.L. and Fyfe, W.S. (1973) The crystallization of magnesite from aqueous solution.
1109 *Geochimica et Cosmochimica Acta*, 37, 87-99.
- 1110 Sayles, F.L. (1979) The composition and diagenesis of interstitial solutions—I. Fluxes across the
1111 seawater-sediment interface in the Atlantic Ocean. *Geochimica et Cosmochimica Acta*,
1112 43, 527–545.
- 1113 Shervais, J.W., Kolesar, P., and Andreasen, K. (2005) *A Field and Chemical Study of*

- 1114 Serpentinization-Stonyford, California: Chemical Flux and Mass Balance. International
1115 Geology Review, 47, 1-23.
- 1116 Siever, R. (1986) Burial Diagenesis of Sandstones. U.S. Geological Survey Bulletin, 1578, 237-
1117 248.
- 1118 Siever, R. (1992) The silica cycle in the Precambrian. *Geochimica et Cosmochimica Acta*, 56,
1119 3265–3272.
- 1120 Spencer, R.J. and Hardie, L.A. (1990) Control of seawater composition by mixing of river waters
1121 and mid-ocean ridge hydrothermal brines. *The Geochemical Society*, 2, 409-419.
- 1122 Stefánsson, A. (2007) Iron(III) Hydrolysis and Solubility at 25 °C. *Environmental Science &*
1123 *Technology*, 41, 6117–6123.
- 1124 Stefurak, E.J.T., Lowe, D.R., Zentner, D., and Fischer, W.W. (2015) Sedimentology and
1125 geochemistry of Archean silica granules. *Geological Society of America Bulletin*,
1126 B31181.1.
- 1127 Stookey, L.L. (1970) Ferrozine---a new spectrophotometric reagent for iron. *Analytical*
1128 *Chemistry*, 42, 779–781.
- 1129 Stüeken, E.E., Kipp, M.A., Koehler, M.C., and Buick, R. (2016) The evolution of Earth’s
1130 biogeochemical nitrogen cycle. *Earth-Science Reviews*, 160, 220–239.
- 1131 Sun, S., Konhauser, K.O., Kappler, A., and Li, Y.-L. (2015) Primary hematite in Neoproterozoic to
1132 Paleoproterozoic oceans. *Geological Society of America Bulletin*, 127, 850–861.
- 1133 Sun, X., Higgins, J., and Turchyn, A.V. (2016) Diffusive cation fluxes in deep-sea sediments and
1134 insight into the global geochemical cycles of calcium, magnesium, sodium and
1135 potassium. *Marine Geology*, 373, 64–77.
- 1136 Suttle, M.D., King, A.J., Schofield, P.F., and Russell, S.S. (2021) The aqueous alteration of CM

- 1137 chondrites, a review. *Geochimica et Cosmochimica Acta*, 299, 219-256.
- 1138 Tomeoka, K., McSween, H.Y., and Buseck, P.R. (1989) Mineralogical Alteration of CM
1139 Carbonaceous Chondrites: A Review. Proceedings of the NIPR Symposium on Antarctic
1140 Meteorites, 2, 221-234.
- 1141 Tosca, N.J., Macdonald, F.A., Strauss, J.V., Johnston, D.T., and Knoll, A.H. (2011) Sedimentary
1142 talc in Neoproterozoic carbonate successions. *Earth and Planetary Science Letters*, 306,
1143 11–22.
- 1144 Tosca, N.J., Guggenheim, S., and Pufahl, P.K. (2016) An authigenic origin for Precambrian
1145 greenalite: Implications for iron formation and the chemistry of ancient seawater.
1146 *Geological Society of America Bulletin*, 128, 511–530.
- 1147 Tosca, N.J., Ahmed, I.A.M., Tutolo, B.M., Ashpitel, A., and Hurowitz, J.A. (2018) Magnetite
1148 authigenesis and the warming of early Mars. *Nature Geoscience*, 11, 635–639.
- 1149 Trendall, A.F. (2002) The Significance of Iron-Formation in the Precambrian Stratigraphic
1150 Record. In W. Altermann and P.L. Corcoran, Eds., *Precambrian Sedimentary
1151 Environments* pp. 33–66. Blackwell Publishing Ltd., Oxford, UK.
- 1152 Trittschack, R., Grobety, B., and Brodard, P. (2014) Kinetics of the chrysotile and brucite
1153 dehydroxylation reaction: a combined non-isothermal/isothermal thermogravimetric
1154 analysis and high-temperature X-ray powder diffraction study. *Physics and Chemistry of
1155 Minerals*, 41, 197-214.
- 1156 Tronc, E., Belleville, P., Jolivet, J.P., and Livage, J. (1992) Transformation of ferric hydroxide
1157 into spinel by iron(II) adsorption. *Langmuir*, 8, 313–319.
- 1158 Tutolo, B.M., Evans, B.W., and Kuehner, S.M. (2019) Serpentine-Hisingerite Solid Solution in
1159 Altered Ferroan Peridotite and Olivine Gabbro. *Minerals*, 47, 1-14.

- 1160 Vacher, L.G., Truche, L., Faure, F., Tissandier, L., Mosser, R., and Marrocchi, Y. (2019)
1161 Deciphering the conditions of tochilinite and cronstedtite formation in CM chondrites
1162 from low temperature hydrothermal experiments. *Meteoritics & Planetary Science*, 54,
1163 1870–1889.
- 1164 Velde, B. (2003) Green Clay Minerals. *Treatise on Geochemistry*, 7, 309-324.
- 1165 Viollier, E., Inglett, P.W., Hunter, K., Roychoudhury, A.N., and Van Cappellen, P. (2000) The
1166 ferrozine method revisited: Fe(II)/Fe(III) determination in natural waters. *Applied*
1167 *Geochemistry*, 15, 785–790.
- 1168 Voigt, M., Pearce, C.R., Fries, D.M., Baldermann, A., and Oelkers, E.H. (2020) Magnesium
1169 isotope fractionation during hydrothermal seawater-basalt interaction. *Geochimica et*
1170 *Cosmochimica Acta*, 272, 21–35.
- 1171 Votyakov, S.L., Chashchukhin, O.L., Galakhova, O.L., and Gulyaeva, T. Y. (2005) Crystal
1172 Chemistry of Lizardite as an Indicator of Early Serpentinization in Ultramafic Rocks I.
1173 Compositional and Structural Features of the Mineral According to Spectroscopic Data.
1174 *Geochemistry International*, 43, 862-880.
- 1175 Walker, J.C.G. (1984) Suboxic diagenesis in banded iron formations. *Nature*, 309, 340–342.
- 1176 Walter, M., Schenkeveld, W.D.C., Reissner, M., Gille, L., and Kraemer, S.M. (2019) The Effect
1177 of pH and Biogenic Ligands on the Weathering of Chrysotile Asbestos: The Pivotal Role
1178 of Tetrahedral Fe in Dissolution Kinetics and Radical Formation. *Chemistry – A*
1179 *European Journal*, 25, 3286–3300.
- 1180 Wicks, F.J., and O’Hanley, D.S. (2018) Chapter 5. Serpentine Minerals: Structures and
1181 Petrology. *Hydrous Phyllosilicates*, 91-168.
- 1182 Zolotov, M.Y. (2014) Formation of brucite and cronstedtite-bearing mineral assemblages on

1183 Ceres. *Icarus*, 228, 13–26.

1184

1185

1186

1187 **Table and Figure Captions**

1188 Table 1. Composition of recreated Archean seawater. Iron and silica concentrations shown as
1189 measured concentrations derived from colorimetric (ferrozine and silicomolybdate) assays where
1190 * denotes the standard deviation of the measurement.

1191
1192 Table 2. pH measurements of Parr vessel precipitates and overlaying solution for control and
1193 bubbled experiments for temperatures that ranged from 25-220 °C. Note pH measurements were
1194 taken after the solution was cooled to 25 °C to minimize temperature effects and the error for
1195 each pH measurement was ± 0.02 pH units.

1196
1197 Table 3: Summary of experimental results of Fe(II) and silica in initial solutions. The measured
1198 Fe(III)/FeT content for the acidified control and bubbled experiments (solution plus precipitate)
1199 after aging in a borosilicate bottle at 25 °C for 19 days.

1200
1201 Table 4. The measured Fe(III)/FeT content by ferrozine and measured Fe(II)/g by vanadate assay
1202 of the acidified control and bubbled solid precipitate from conditions ranging 25-220 °C over 19-
1203 40 total days.

1204
1205 Table 5. Summary of the average elemental composition of the phases (in atomic % or as a ratio)
1206 at each experimental condition. Also see the raw EDS data for each experiment in Table S3.

1207
1208 Figure 1: Time-temperature scheme for hydrothermal aging of control and bubbled experiments.
1209 The reaction with O₂ and equilibrium period took place in borosilicate bottles denoted by the

1210 light gray region. Control and bubbled experiments were subsampled for pH and Fe(III)/FeT
1211 after 19 days at room temperature (star symbol). The remainder of material was portioned and
1212 transferred into anoxic Parr vessels for aging at 25, 80, 150, and 220 °C before being sampled
1213 and analyzed (filled circles).

1214

1215 Figure 2: (a) Plot of pH measurements from Parr vessel with precipitate and overlaying solution
1216 for control and bubbled experiments for temperatures that ranged from 25 - 220 °C. Note the
1217 uncertainty of the pH measurements and oven temperatures was ± 0.02 pH units and ± 0.4 °C
1218 respectively. (b) The measured Fe(III)/FeT content of the acidified control precipitates and
1219 bubbled precipitates along with the calculated standard deviation from replicate measurements.

1220

1221 Figure 3: Cobalt sourced XRD patterns from replicate bubbled experimental precipitates subject
1222 to simulated diagenesis at 25 °C (Blue), 80 °C (Green), 150 °C (Black), and 220 °C (Red).

1223 Plotted for comparison: blank kapton tube (K); 1:1 iron-silicates greenalite (G),

1224 $[\text{Fe}^{2+}_3\text{Si}_2\text{O}_5(\text{OH})_4]$ (from Guggenheim et al. 1982) and cronstedtite (C),

1225 $[(\text{Fe}^{2+}, \text{Fe}^{3+})_3(\text{Si}, \text{Fe}^{3+})_2\text{O}_5(\text{OH})_4]$ (Lab Standard, Caltech Mineralogical Collection); a spinel group

1226 iron-oxide, magnetite (M), $[\text{Fe}^{2+}\text{Fe}^{3+}_2\text{O}_4]$ (from Haavik et al. 2000); and 6-line ferrihydrite (F)

1227 $[\text{Fe}^{3+}_{10}\text{O}_{14}(\text{OH})_2]$ (from Michel et al. 2007). Both the copper and cobalt two theta axes are plotted

1228 for comparison. The experimental and standard diffraction patterns were vertically offset for

1229 clarity.

1230

1231 Figure 4: The precipitate from the 150 °C control experiment had a tan color (**a-left**) and was

1232 moderately attracted to the magnet (**a-right**). The precipitate from the 220 °C control experiment

1233 continued to have a tan color (**b-left**) but only some particles appeared to be attracted to the
1234 magnet (**b-right**). The precipitate from the bubbled experiment after aging at 25 °C had a green
1235 color (**c-top**) and was not attracted to the magnet (**c-bottom**). The bubbled experiment harvested
1236 after aging at 80 °C was green (**d-top**) and was moderately attracted to the magnet (**d-bottom**).
1237 The bubbled 150 °C precipitate was dark green (**e-top**) and continued to be moderately attracted
1238 to the magnet (**e-bottom**). The bubbled 220 °C precipitate was darker green (**f-top**) and was
1239 highly attracted to the magnet (**f-bottom**).

1240

1241 Figure 5: Tan precipitate harvested from control experiment after 7 days at 150 °C (**a**). Clumps
1242 of heterogeneous particles (**b-c**) included poorly formed tubular spindles (**c-d**) and faint poorly
1243 crystalline globular masses (**d-arrows**). Some of these particles were primarily composed of Mg-
1244 Si-Fe (**e**, Tables 5 and S3) and appeared to be layered structures with frayed edges with two
1245 particles showing 6.9 Å and 7.2 Å lattice spacings (**f**). Other globular particles did not show
1246 layering but had lattice spacings including 1.5 Å (**f**), 2.3 Å (**g**), and 2.5 Å (**g-I**). In other regions,
1247 we observed blunt-edged rods intermixed with masses of minute globules (**h**) with both
1248 containing Fe- and O-rich measured elemental chemistry (**i-j**; Table 5). Basal spacing of the
1249 blunt-edge rods was measured to be 6.2 Å (**k**), similar to another phase with a lathe-like
1250 morphology (**l**) with 3.2 Å and 6.1 Å lattice spacing (**l-I & l-II**). The polynanocrystalline SAED
1251 pattern from a region containing blunt-edged rods and lathes was most consistent with
1252 lepidocrocite (**m**).

1253

1254 Figure 6: Tan precipitate harvested from control experiment after aging for 7 days at 220 °C (**a**).
1255 Homogenous clumps composed of hollow tubes (**b-d**) and measured elemental chemistry (**e**).

1256 Viewing down the tube axis and along the profile of the tube we measured the lattice spacing to
1257 be 7.2 Å in both instances (**f & g-I**) and measured 4.3 Å at a different orientation (**g-II**). A
1258 globular phase was observed (**h**) with elemental chemistry rich in Fe and O (**i**). SAED of a region
1259 containing both the tubular and globular phase respectively produced a polynanocrystalline
1260 pattern consistent with a magnesium-silicate and planes for a spinel group phase (**j**).

1261

1262 Figure 7: Subtle globular phase observed in all bubbled experiments and tentatively identified as
1263 ferrihydrite. At 25 °C, TEM imaging captured a faint background, webbing-like phase (**a-**
1264 **arrows**) and SAED of the region showed diffuse halos corresponding to 1.3 Å, 1.5 Å, and 2.6 Å
1265 lattice spacings (**b**). HR-TEM and IFFT analysis of this phase identified a lattice spacing of 2.6
1266 Å (**c, c-I, c-II**). Similarly, we observed a globular phase at 80 °C (d-e) with a major spacing at
1267 2.5 Å and 2.6 Å (**e-I, e-II**). An image of the bubbled precipitate at 150 °C showed an aggregate
1268 of small globules (**e-f**) and analysis of this ‘background’ phase showed 1.6 and 2.6 Å spacing (**g-**
1269 **I, g-II**). After 220 °C aging, TEM imaging continued to show faint round morphologies (**h-i**)
1270 with 2.6 Å lattice spacing (**i-II**).

1271

1272 Figure 8: After hydrothermal aging, we observed a plate-like phase that often had a triangular or
1273 polygonal shape, ultimately identified as magnetite. One TEM image of the 80 °C sample
1274 showed all three phases that we observed, including triangular platelets (**a-arrows**). This phase
1275 was also identified intermixed with layered structures (**b**) where we measured a 4.7 Å lattice
1276 fringe (**c**) and multiple FFT lattice spacings corresponding to a spinel group phase such as
1277 magnetite (**c-I**). We also observed a platelet phase after the 150 °C hydrothermal treatment (**d-**
1278 **arrows, e**) with 4.7 Å lattice spacing (**f**) where FFT confirmed the presence of lattice planes

1279 consistent with a spinel group mineral (**f-I**). Additionally, we obtained iron- and oxygen-rich
1280 elemental chemistry on a platelet phase after 220 °C aging (**g**) and measured 4.7 Å lattice
1281 spacing (**h**) and FFT lattice planes consistent with a spinel group identification (**h-I**). SAED of
1282 an area containing the platelets displayed polynanocrystalline halos at the lattice planes of a
1283 spinel group mineral (**i**).

1284

1285 Figure 9: TEM-based observations of poorly layered structures from green precipitate (**a**)
1286 harvested from the bubbled experiment held at 25 °C for 40 days. We saw abundant particles
1287 with a spindly morphology in clusters (**b-d**) where we mapped and analyzed their elemental
1288 chemistry (**e-g**), finding the major elements were Fe, Si, and O with minor Mg. Note that the
1289 average compositions shown in (**f**) and (**g**) are from hand-drawn regions to pick out the layered
1290 particles, and the chemistry in (**g**) derives from the interior silicate-rich portion of the aggregate.
1291 The best captured particles exhibited a maximum of 3-4 layers (**h-i**) with an approximate basal
1292 spacing of ~7.2-7.7 Å determined by IFFT (**h-I, h-II, i-I, & i-II**).

1293

1294 Figure 10: TEM analyses of green precipitate (**a**) harvested from the bubbled experiment after 7
1295 days at 80 °C, focusing on the layered structures. We observed a heterogeneous mixture of
1296 morphologies, including well-ordered blades (**b-e**) with the elemental chemistry maps shown for
1297 Fe, Si, Mg, and O (**d**) and average chemistry shown in (**e**). There were also trapezoidal structures
1298 (**b-arrows, f-g, i-j**) with similar chemistry rich in Fe, Si, and O (chemistry shown from “caps” of
1299 structures). The blades showed a 7.2 Å lattice fringe (**h**), while the trapezoidal structure’s “body”
1300 (**i**) had frequent crystal defects (**i-arrows**) but still contained 7.2 Å lattice spacing (**i-I**). The well-
1301 crystallized “caps” of the trapezoidal structure (**j**) had 7.0 Å and 2.1 Å lattice spacing (**j-I & j-II**)

1302 while SAED of a heterogeneous area similar to panel b produced recurring lattice planes
1303 consistent with a serpentine group phase (**k**).

1304

1305 Figure 11: Layered phase observations from the dark green precipitate (**a**) harvested from the
1306 bubbled experiment after 7 days at 150 °C. TEM revealed a heterogeneous mixture of phases (**b**)
1307 including well-ordered blades (**c-f**) where the elemental chemistry of the layered blades indicated
1308 a phase rich in Fe and Si with around 5% Mg (**e-g**; Table 5). Lattice spacings of this layered
1309 phase were measured to be 7.2 Å (**h**) and 7.3 Å (**h-I**), with some particles showing not only the
1310 basal lattice spacing (001) 7.1 Å (**i**) but also a 24 Å superlattice modulation (**i-I**).

1311

1312 Figure 12: Layered structures in the bubbled experiment after 7 days at 220 °C, which yielded
1313 the darkest green-black precipitate (**a**). TEM revealed the heterogeneous phases (**b**) within this
1314 experiment that included well-ordered blades with a 7.1 Å lattice spacing (**c**) along with
1315 elemental chemistry rich in Fe, Si, and Mg (**d**). An additional example of this layered, bladed
1316 phase (**e**) showed a 7.1 Å d-spacing (001) with superlattice modulation of 21 Å (**f & f-I**), and
1317 similar elemental chemistry (**g**).

1318

1319 Figure 13: Compilation of the layered phase observed in bubbled experiments at temperatures
1320 25, 80, 150 and 220 °C. At 25 °C, we observed spindly particles (**a**) with a maximum of 4 layers
1321 (**a-I**) measured as having an approximate lattice spacing of 7.7 Å by IFFT (**a-II**) with FFT only
1322 showing the basal d-spacing (001) (**a-III**). Cluster of poorly layered particles in HAADF (**a-IV**)
1323 shows Mg distribution and content on average (**a-V**). At 80 °C, we observed well-ordered
1324 particles (**b**) with extensive layering (**b-I**) with a lattice fringe of 7.2 Å as measured by IFFT (**b-**

1325 **II)** and showing multiple lattice planes by FFT (**b-III**). Region with well-ordered layered blades
1326 in HAADF (**b-IV**) and Mg distribution and average content (**b-V**). We observed similar well-
1327 ordered particles at 150 °C (**c**) with extensive layering (**c-I**) where the lattice fringe was 7.1 Å by
1328 IFFT (**c-II**) and displayed recurring lattice planes by FFT (**c-III**). Collection of well-ordered
1329 particles in HAADF (**c-IV**) alongside Mg distribution and content (**c-V**). At 220 °C, we
1330 continued to observe a well-ordered layered phase (**d & d-I**) with a measured lattice fringe of 7.1
1331 Å by IFFT (**d-II**) and recurring lattice planes by FFT (**d-III**). Collection of well-ordered particles
1332 in HAADF (**d-IV**) and Mg distribution and content (**d-V**).
1333

1334 **Main Text Tables**1335 **Table 1**

Chemical Component, Chemical Formula	Concentration [mM]
Sodium chloride, NaCl	400
Sodium bicarbonate, NaHCO ₃	30
Magnesium chloride hexahydrate, MgCl ₂ * 6H ₂ O	10
Ammonium chloride, NH ₄ Cl	10
Potassium chloride, KCl	7
Sodium orthosilicate, Na ₄ SiO ₄	1.1 ± 0.08*
Ferrous chloride tetrahydrate, FeCl ₂ * 4H ₂ O	1.1 ± 0.09*
Total cation equivalents from salts (est. from acid/base)	473.6 (500)
Total anion equivalents from salts (est. from acid/base)	473.6 (480-490)

1336

1337

1338

1339

1340

1341

1342

1343 **Table 2**

1344

Temperature (°C)	Time (Days)	Bubbled (pH)	Control (pH)
25	19	7.33	7.14
25	40	7.06	7.17
80	7 (26)	6.74	6.92
150	7 (33)	6.41	6.43
220	7 (40)	5.85	7.65

1345

1346 **Table 3**

Condition	Measurement \pm Standard Deviation
Silica in initial solution [mM]	1.1 \pm 0.08
Fe(II) in initial solution [mM]	1.1 \pm 0.03
<u>Fe[III]</u> (bulk) of acidified control after 19 days 25 °C FeT	0.07 \pm 0.02
<u>Fe[III]</u> (bulk) in acidified bubbled exp after 19 days 25 °C FeT	0.75 \pm 0.05

1347

1348

1349 **Table 4**

Condition	$\frac{\text{Fe[III]}}{\text{FeT}}$ (Ferrozine)	% Fe(II)/g (vanadate)
Control solids after 7 days 150 °C (33 days total)	0.27 ± 0.9	
Control solids after 7 days 220 °C (40 days total)	0.32 ± 2	
Bubbled solids after 19-21 days 25 °C	0.48 ± 0.06	48.14
Bubbled solids after 40 days 25 °C	0.45 ± 1.8	
Bubbled solids after 7 days 80 °C (26 days total)	0.45 ± 2.5	55.85
Bubbled solids after 7 days 150 °C (33 days total)	0.51 ± 0.06	32.22
Bubbled solids after 7 days 220 °C (40 days total)	0.46 ± 2.4	27.92

1350

1351

1352

1353

Table 5

	Average Atomic %					Elemental Ratios		
Experimental Condition	Fe	Mg	Si	Al	O	avg Fe/(Fe+Mg)	avg (Fe+Mg)/Si	range (Fe+Mg)/Si
Bubbled 25C Poorly Layered	19.94	2.00	17.91	0.96	59.19	0.91	1.23	1.06-1.34
Bubbled 25C Mixed poorly crystalline oxides, layered, salts	18.96	1.83	18.04	1.73	59.45	0.91	n.a.	n.a.
Bubbled 80C Well Ordered Layered	27.70	1.61	12.94	1.03	56.73	0.95	2.27	2.11-2.43
Bubbled 150C Well Ordered Layered	22.13	4.54	14.91	0.77	57.65	0.83	1.79	1.59-2.14
Bubbled 220C Well Ordered Layered	16.22	10.02	15.23	0.87	58.01	0.62	1.72	1.6-1.85
Bubbled 220C Spinel Group Oxide	22.44	9.17	10.68	1.59	56.13	0.71	n.a.	n.a.
Control 150C Poorly Layered	8.58	17.35	15.50	0.65	57.91	0.33	1.67	1.45-1.67
Control 150C Iron Oxide Mass	31.08	4.17	7.89	2.33	54.53	0.88	n.a.	n.a.
Control 150C Iron Oxide Rods	28.54	7.13	7.39	2.59	54.34	0.80	n.a.	n.a.
Control 220C Well Ordered Layered	4.78	28.84	10.21	0.85	55.32	0.14	3.29	3.29
Control 220C Spinel Group Oxide	27.81	9.24	7.40	1.48	54.07	0.75	n.a.	n.a.

Figure 1

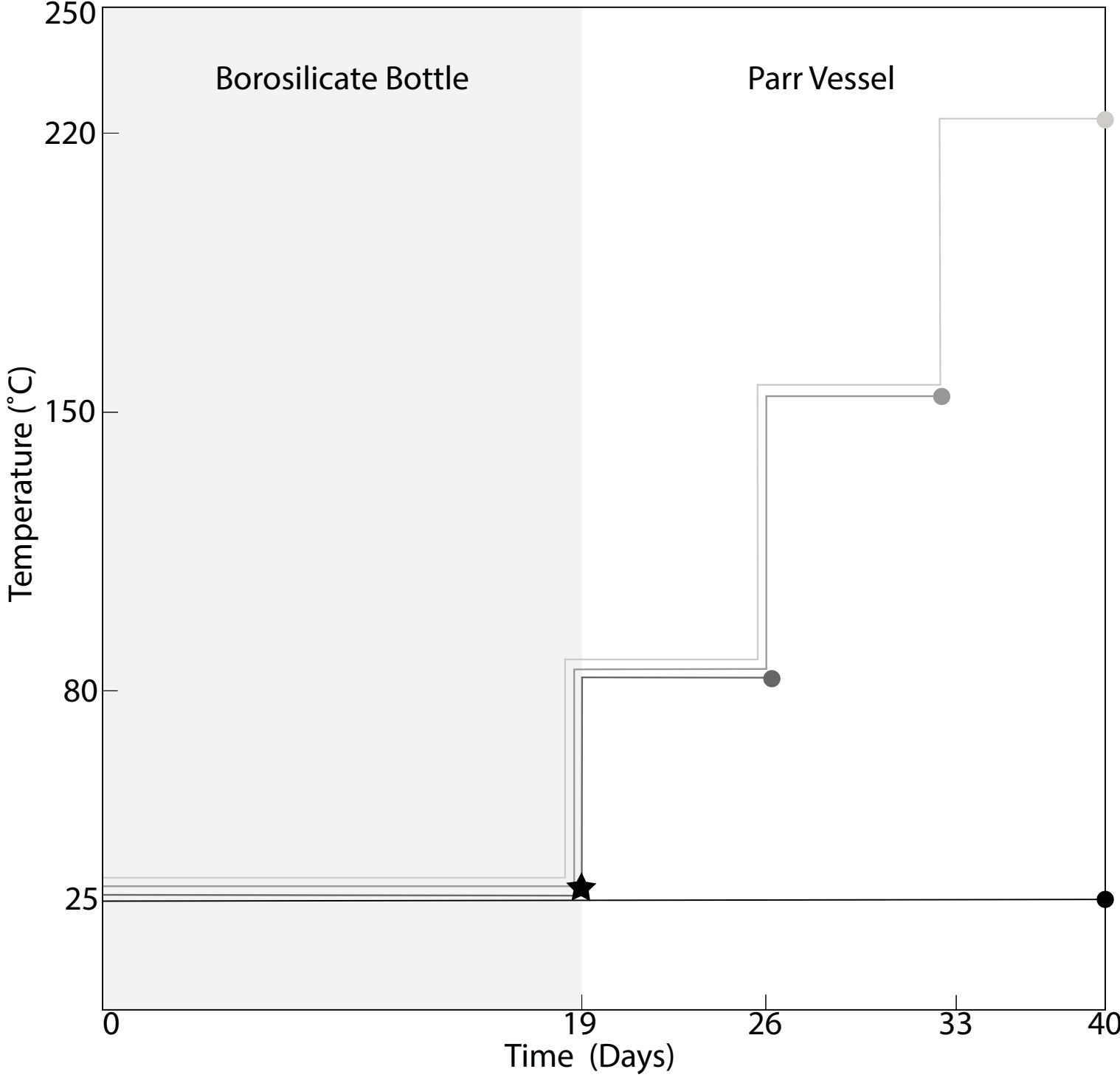


Figure 2

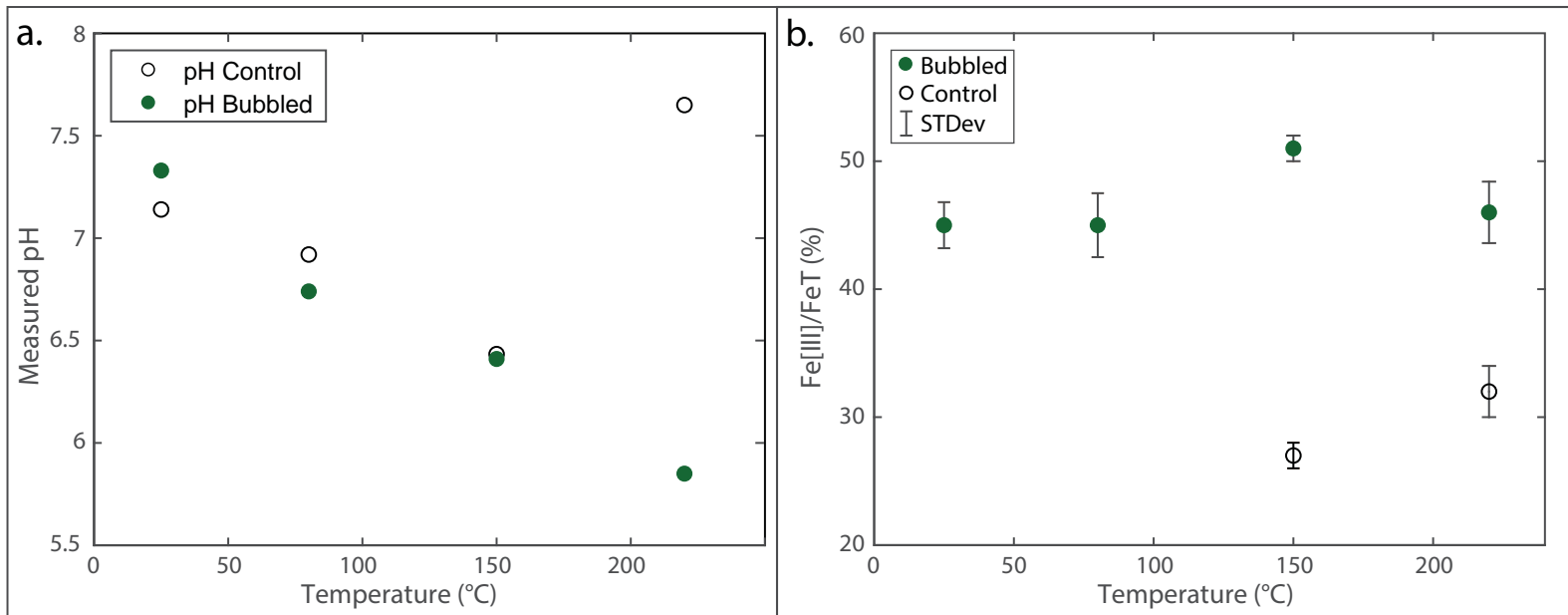


Figure 3

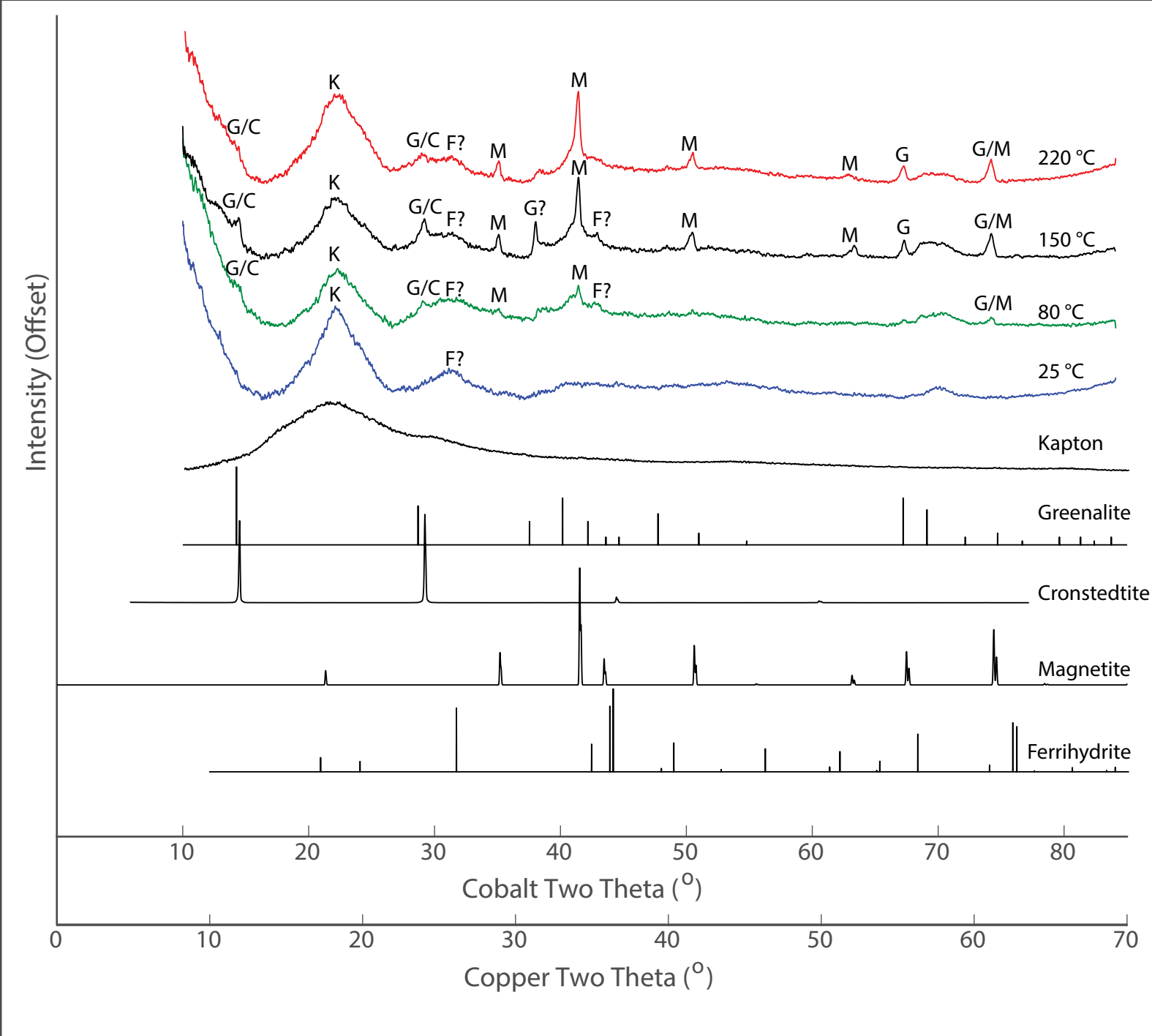


Figure 4

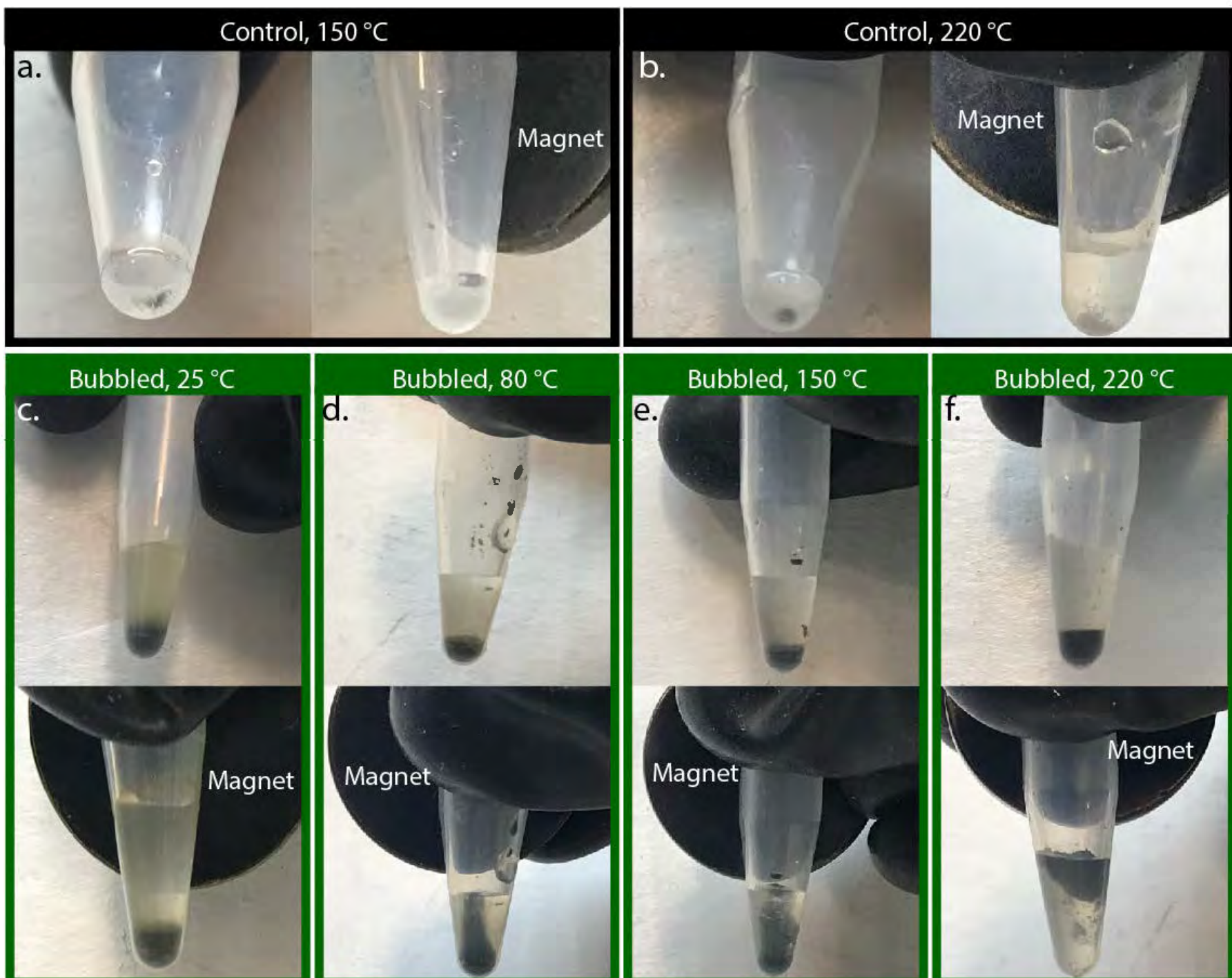


Figure 5

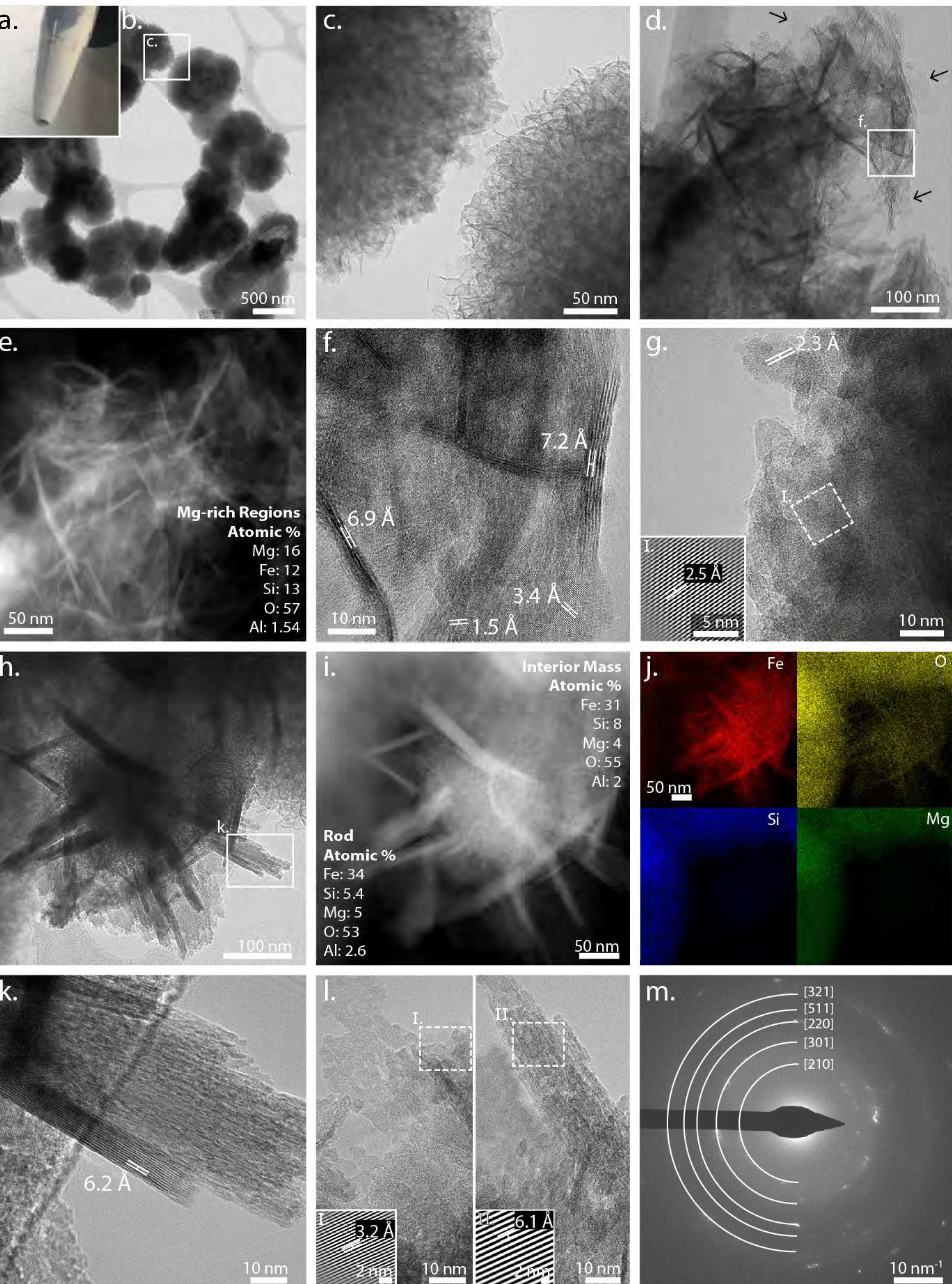


Figure 6

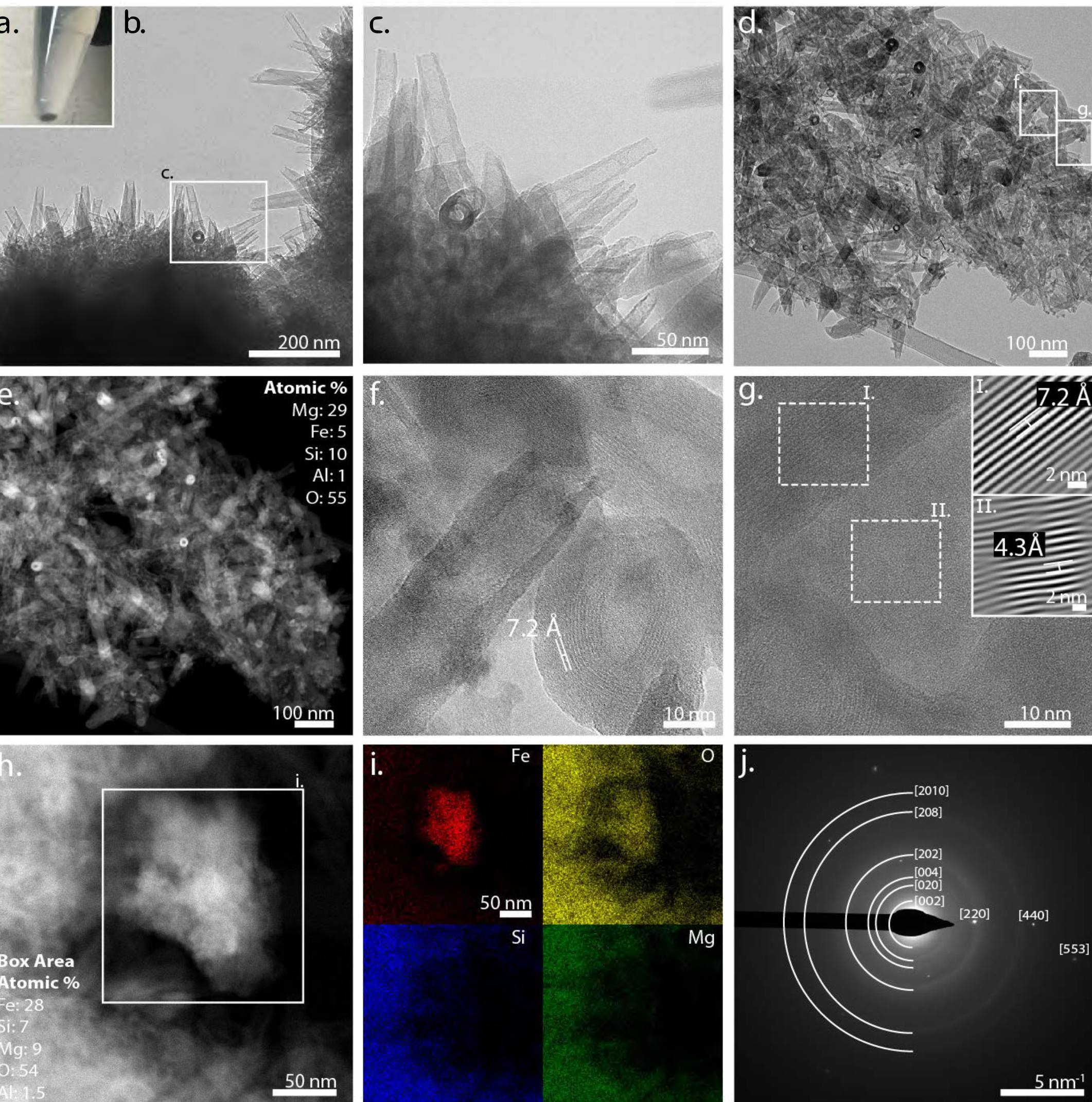


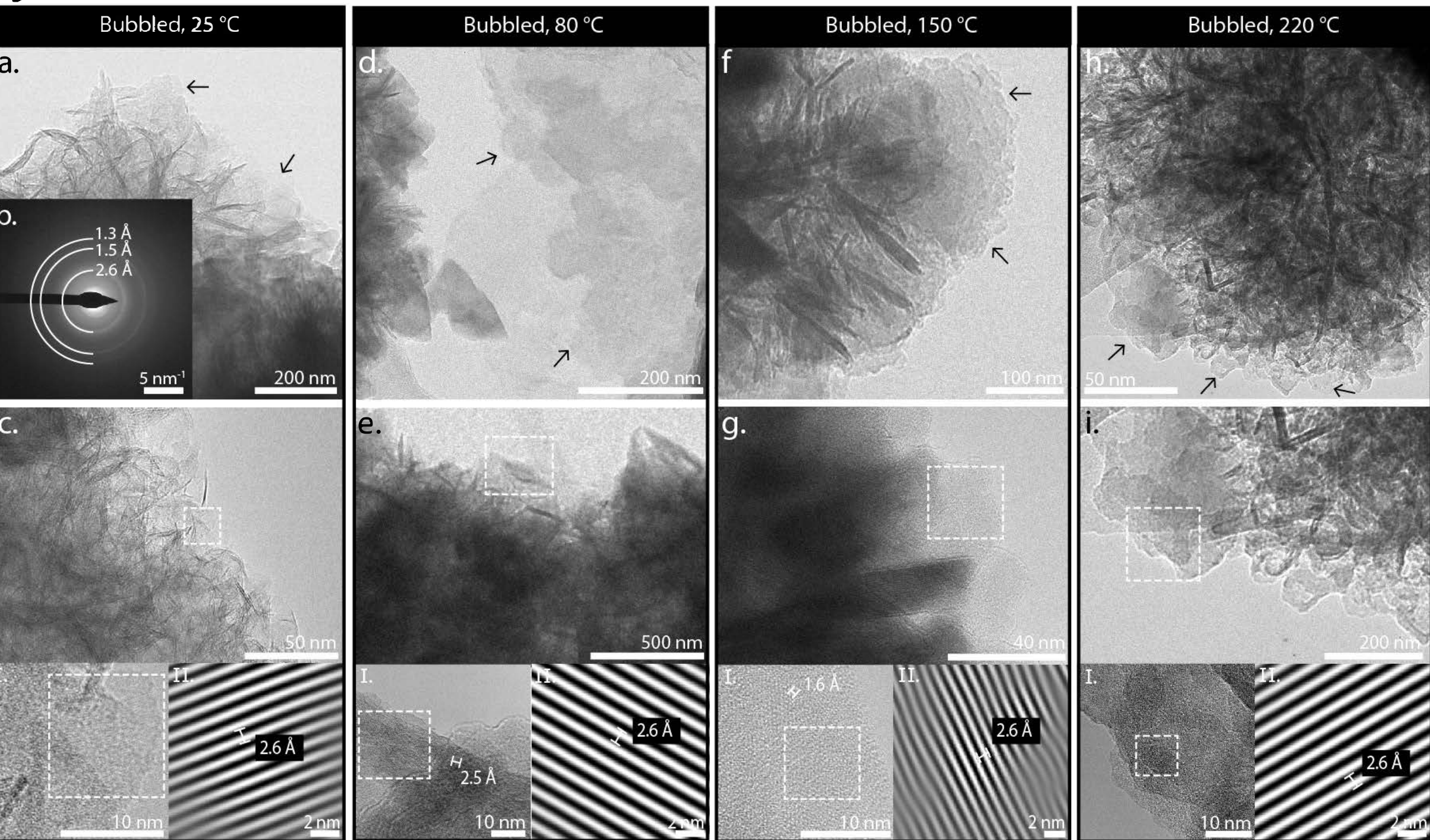
Figure 7

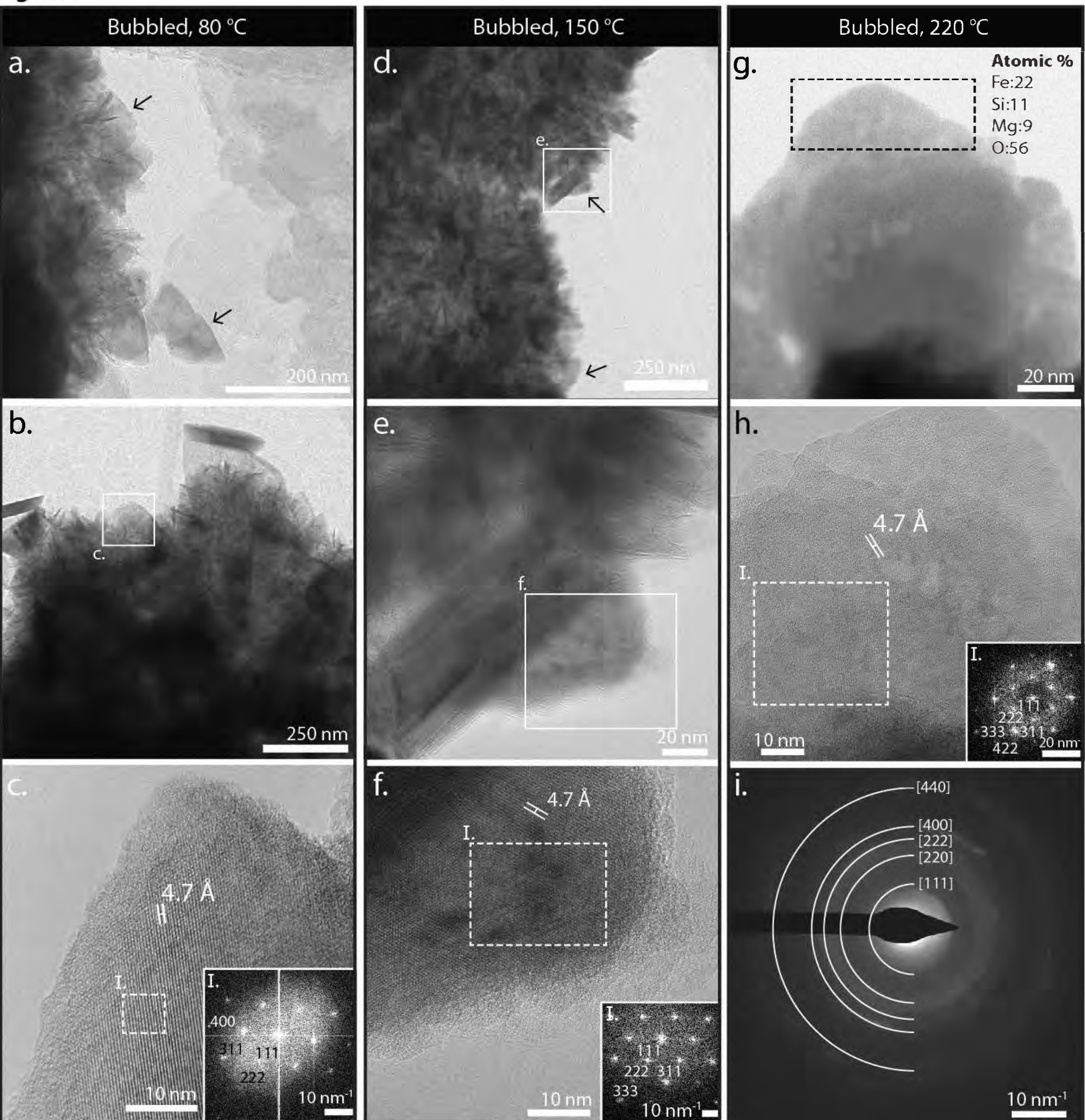
Figure 8

Figure 9

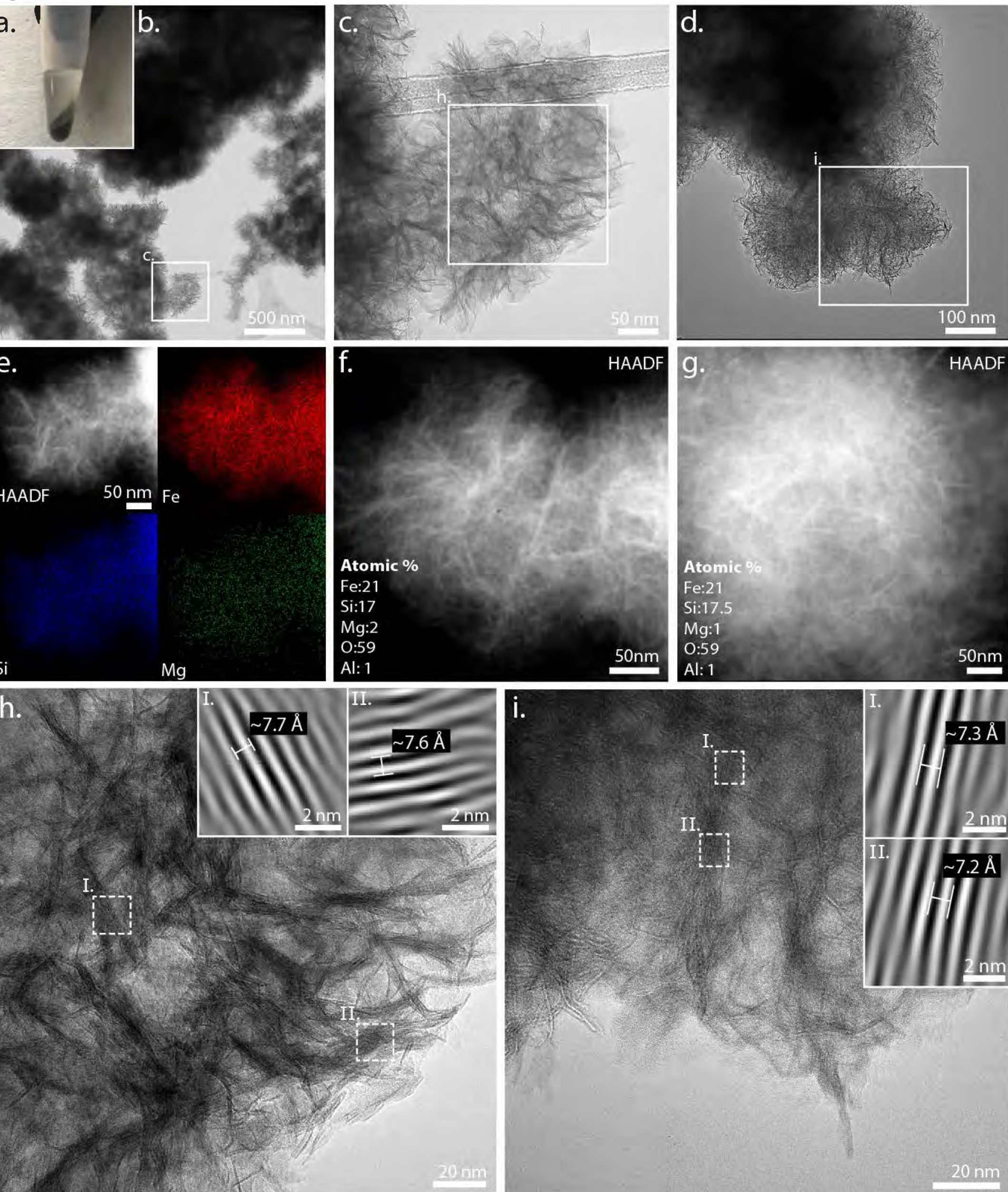


Figure 10

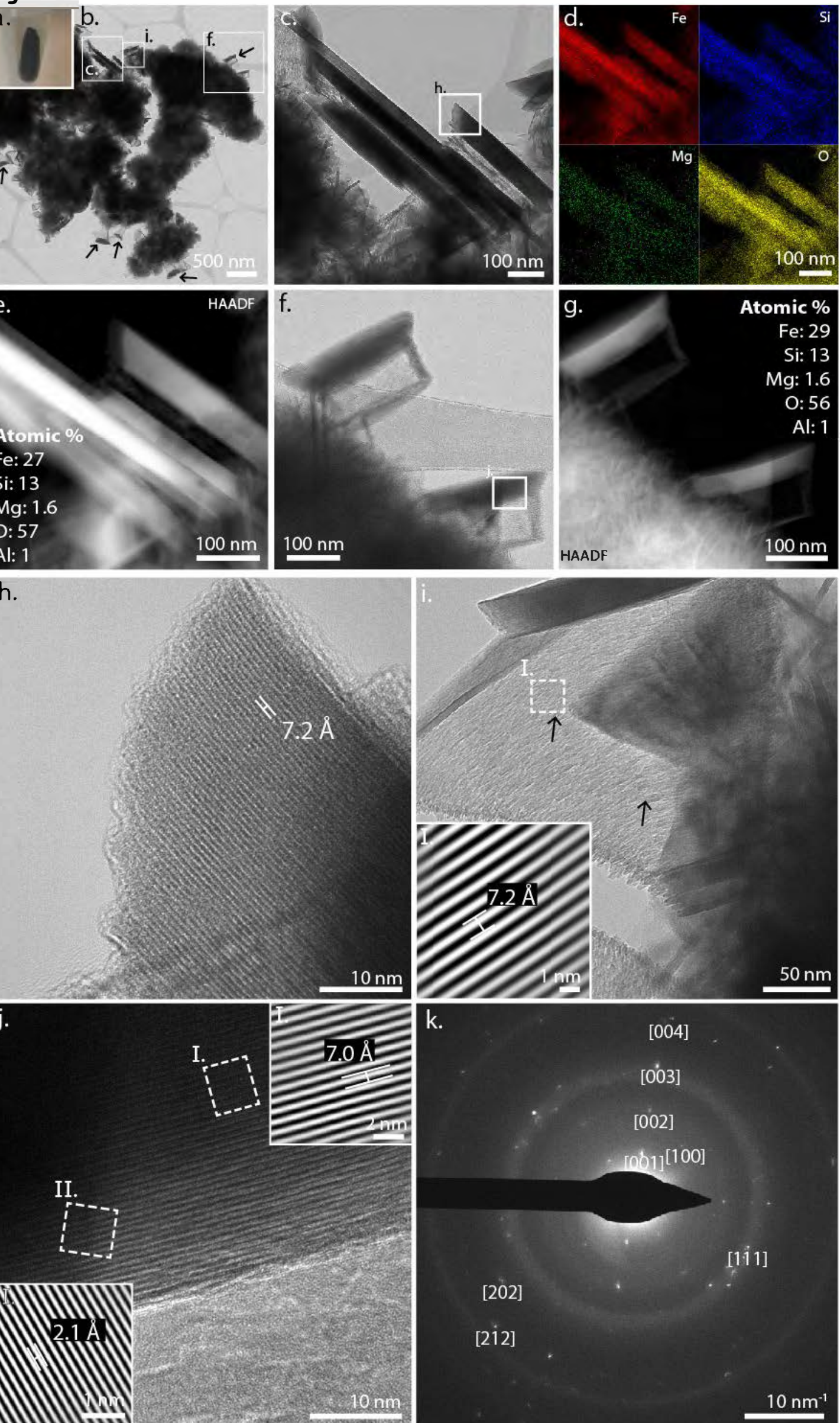


Figure 11

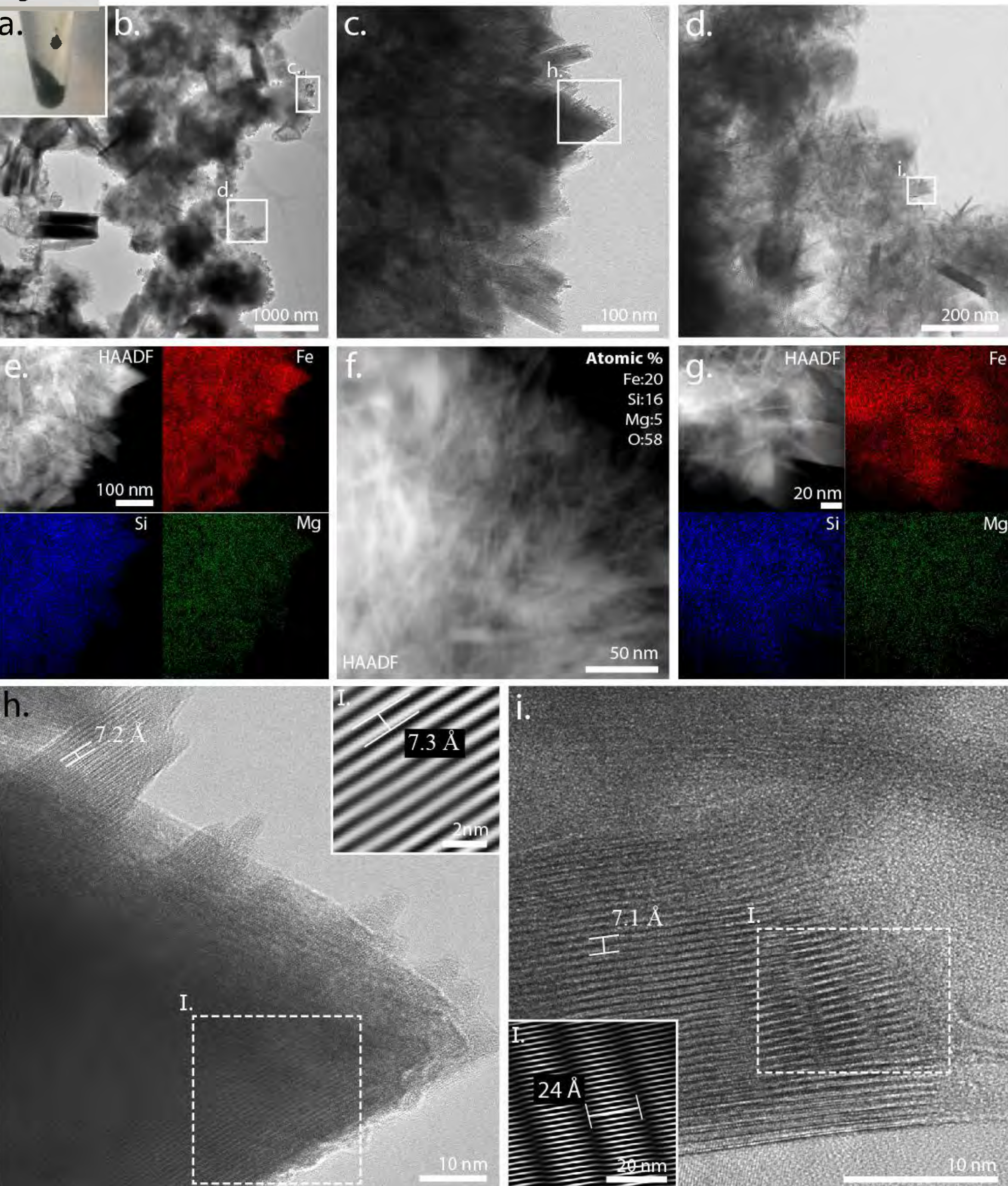


Figure 12

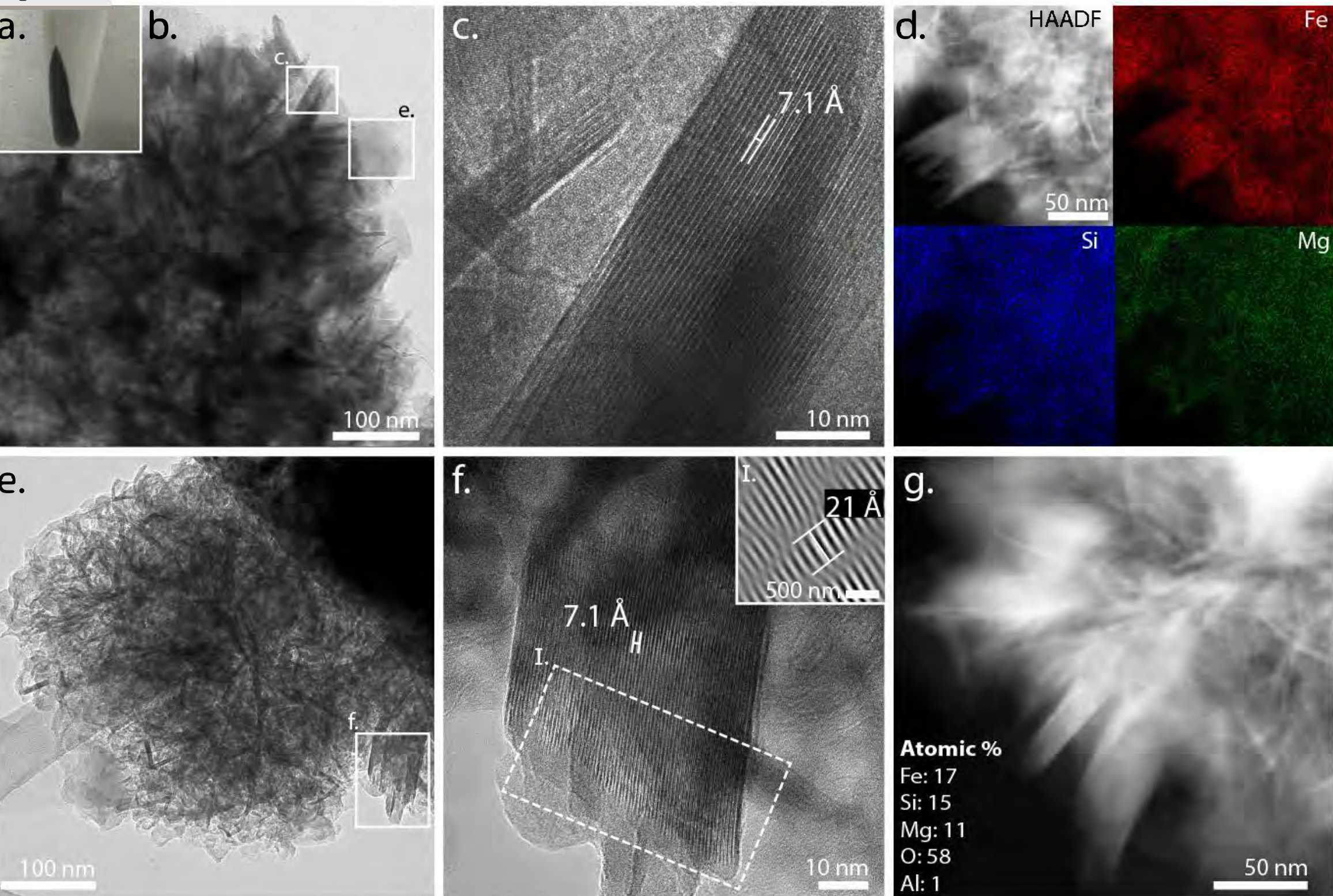


Figure 13